

## Article

# Structural Performance of Energy Efficient Geopolymer Concrete Confined Masonry: An Approach towards Decarbonization

Muhammad Mubashir Ajmal <sup>1</sup>, Asad Ullah Qazi <sup>1</sup>, Ali Ahmed <sup>1</sup>, Ubaid Ahmad Mughal <sup>1</sup>, Safeer Abbas <sup>1,\*</sup>, Syed Minhaj Saleem Kazmi <sup>2,\*</sup> and Muhammad Junaid Munir <sup>2</sup>

<sup>1</sup> Department of Civil Engineering, University of Engineering and Technology, Lahore 54890, Pakistan; mmubashirajmal@gmail.com (M.M.A.); asad.qazi@uet.edu.pk (A.U.Q.); ali@uet.edu.pk (A.A.); ubaid\_mughal@uet.edu.pk (U.A.M.)

<sup>2</sup> School of Engineering, RMIT University, Melbourne, VIC 3001, Australia; muhammad.munir@rmit.edu.au

\* Correspondence: safeer.abbas@uet.edu.pk (S.A.); minhajkazmi17@gmail.com (S.M.S.K.)

**Abstract:** Geopolymer concrete is preferred over OPC due to its use of energy waste such as fly ash, making it more sustainable and energy-efficient. However, limited research has been done on its seismic characterization in confined masonry, highlighting a gap in sustainable earthquake-resistant structures. Our study compares the performance of alkali-activated fly-ash-based geopolymer concrete bare frame and confined masonry wall panels with conventional concrete. Experimental results showed that geopolymer concrete bare frame has 3.5% higher initial stiffness and 1.0% higher lateral load-bearing capacity compared to conventional concrete. Geopolymer concrete confined masonry exhibited 45.2% higher initial stiffness and 4.1% higher ultimate seismic capacity than traditional concrete. The experimental results were verified using a numerical simulation technique with ANSYS-APDL, showing good correlation. Comparison with previously tested masonry walls revealed that GPC confined masonry has similar structural behavior to cement concrete masonry. This study demonstrates that geopolymer concrete made from waste energy such as fly ash is a sustainable and low-energy substitute for OPC concrete, particularly in highly seismic-prone areas, for a cleaner environment.

**Keywords:** GPC confined masonry; GPC bare frame; reverse cyclic loading; ANSYS; numerical simulation



**Citation:** Ajmal, M.M.; Qazi, A.U.; Ahmed, A.; Mughal, U.A.; Abbas, S.; Kazmi, S.M.S.; Munir, M.J. Structural Performance of Energy Efficient Geopolymer Concrete Confined Masonry: An Approach towards Decarbonization. *Energies* **2023**, *16*, 3579. <https://doi.org/10.3390/en16083579>

Academic Editor: Izabela Hager

Received: 31 March 2023

Revised: 16 April 2023

Accepted: 19 April 2023

Published: 20 April 2023



**Copyright:** © 2023 by the authors. Licensee MDPI, Basel, Switzerland. This article is an open access article distributed under the terms and conditions of the Creative Commons Attribution (CC BY) license (<https://creativecommons.org/licenses/by/4.0/>).

## 1. Introduction

Load-bearing masonry has been the most widely used construction technology worldwide since the beginning of building construction because of its affordability, ease of implementation, and eco-friendly features [1]. However, these, non-engineered construction practices have led to a significant increase in the seismic hazard posed by masonry caused by inherent deficiencies such as low tensile strength of masonry and weak connections between elements. Therefore, poor design and detailing can result in buildings that are susceptible to earthquake damage [2,3]. Unreinforced masonry structures perform well when subjected to gravity load, due to the reasonable compressive strength of masonry units, but on the other hand, it becomes a challenge for the engineers to enhance the tension and shear capacity of masonry structures to achieve improved sustainability during seismic excitations [4,5]. Unreinforced masonry still finds broad use in existing structures across most seismic regions. The assessment of the seismic vulnerability of such buildings is of critical significance. Indeed, said buildings have exhibited poor behavior under past earthquakes resulting in massive damage, structural failure, and casualties [6]. Japan, China, Indonesia, Italy, Iran, India, and Pakistan are a few of the earthquake-prone regions, which have suffered huge losses in past ground shakes [7].

A recent earthquake (October 2005 AJK) has highlighted the vulnerability of masonry structures and resulted in substantial devastation and thousands of people losing their

lives. The same earthquake left extensive destruction, snatching the lives of more than 73,000 people, ruthlessly injuring another 70,000, and making 2.8 million people shelter-less with over 450,000 buildings fully or partially damaged [8]. The major causes of destruction encompassed the fragile interlocking bond between out-of-plane and in-plane walls, low quality of building material, and non-engineered construction practices [9].

To address these challenges, the implementation of modern seismic design codes can help assess the mechanical response of both new and existing structures, thus improving their resilience to seismic activity. Confined masonry (CM) is one of the best reinforcing masonry wall systems. It was introduced in Italy and Chile in the wake of disastrous earthquakes, namely the 1908 Messina and 1929 Talca quakes, respectively [10]. Confined masonry, which is widely used for housing in Mexico [11] and most Latin-American countries [12–15], is also a common construction technique in several European countries such as Italy, Portugal, and Slovenia [16–18], as well as Asian countries including Iran [19,20], Indonesia [21], Pakistan [22], and China [16,23]. In areas with moderate to high seismic activity, confined masonry has been used as a common building technique for low- to mid-rise structures [24,25]. Confined masonry is a structural technique that improves the load-bearing capacity of masonry walls against both vertical and lateral loads by using tie-beams and tie-columns [26,27].

Seismic performance of confined masonry has been, undoubtedly, proved to be far better than non-engineered conventional masonry structures [28–33]. At the same time, the confined masonry does consist for the most part of cement-based materials, i.e., concrete, and mortar, representing a vital ingredient in the construction industry [34,35]. The manufacturing of OPC results in significant emissions of anthropogenic carbon dioxide that contribute towards global warming [36–41]. The International Energy Agency reports that the manufacturing of OPC accounts for approximately 5–7% of global greenhouse gas emissions and lays the foundation for the onset of global warming [42–46]. The Geological Survey (2012) estimated that global OPC production is currently around 3.6 billion metric tons, and projections suggest that it will exceed 5 billion metric tons in the near future [47]. Typically, manufacturing one ton of Portland cement (PC) needs approximately 1.5 tons of raw materials, which results in the emission of approximately 0.9 tons of CO<sub>2</sub> [48–51].

Over the last twenty years, considerable research efforts have been focused on finding substitutes for OPC concrete. Geopolymer concrete (GPC) is one such alternative that can be made using industrial waste materials such as fly ash and slags [52–54]. Recently, geopolymer concrete has gained significant attention due to its potential to serve as a replacement for ordinary Portland cement, leading to a substantial reduction in carbon dioxide emissions [55]. GPC achieves strength through the polymerization process [56]. The reaction of aluminosilicate materials with a highly alkaline solution results in the development of geopolymeric gel [57]. Past studies show that GPC can be produced using fly ash [58], metakaolin [59], silica fume [60], ground granulated blast furnace slag [61], and rice husk ash [62], among which fly ash is the most used waste material to produce GPC due to its superior engineering and durability properties [63]. Furthermore, it is pertinent to mention that both types of concrete are heterogeneous and their physical properties at meso-scale may also impact the behavior that can be studied utilizing micro X-ray computed tomography images [64].

Geopolymer concrete has been proven to be appropriate for use in Civil engineering projects such as constructing roads, footpaths, and pipes. However, before it can be widely used in structural applications and the establishment of national codes of practice, further testing is necessary to assess its overall structural performance. Currently, most of the research on geopolymer concrete has focused on material development and mechanical behavior measurement [65–71], with relatively few studies examining the behavior of geopolymer concrete in structural elements [72–75].

Geopolymer concrete offers several environmental, structural, and economic advantages over traditional concrete, but the available literature is mostly limited to geopolymer concrete elements and very little research has been extended to reinforced geopolymer con-

crete members (beam/column/slab). However, no studies are yet reported on the seismic characterization of geopolymer concrete confined masonry using fly ash as a precursor, which highlights a huge gap in the research needed to produce a clean green environment in highly seismic-prone regions. Therefore, it is a pressing need to study the seismic resilience of geopolymer concrete at the structure level in the form of confined masonry.

This paper provides a comprehensive study on the alkali-activated fly-ash-based geopolymer concrete bare frame under reverse cyclic load and its comparison with conventional concrete. Upon successful concordance, the research has been extended to the comparison of the structural performance of GPC confined masonry with that of cement concrete. Benchmark walls tested under lateral in-plane loading are used to calibrate a finite element modeling approach for reverse cyclic analysis. For this purpose, a numerical solution based on the finite element method has been carried out to model the test results. A comparison has also been drawn among the test specimens in this study and previously tested confined and unreinforced masonry walls to estimate the difference of important seismic parameters of GPC confined masonry compared with that of cement concrete masonry. The present experimental and numerical observations and results make the basis for further testing on fly-ash-based geopolymer concrete confined masonry rooms to study different lateral and torsional behaviors to produce a green environment, especially in seismic-prone areas.

## 2. Methodology

### 2.1. Experimental Setup

#### 2.1.1. Test Specimens and Geometric Properties

The test specimens presented in this study are bare frame and confined masonry made with alkali-activated fly-ash-based geopolymer concrete and their comparison with the conventional concrete. All the test specimens were subjected to the quasi-static reverse cyclic load. The nominal dimension of the bare frames and single wythe confined masonry walls are 1870 mm × 1850 mm × 113 mm (length × height × width). In order to prioritize shear failure over flexural failure, the aspect ratio of both bare frames and walls was kept approximately equal to 1.0. A reinforced concrete pad measuring 2470 mm × 300 mm × 300 mm (length × width × depth) was used to construct the specimen, simulating a sturdy foundation for the sample. The footing beam extended 300 mm on each side of the main structure to anchor the specimen with the testing floor, preventing any sliding or uplift at the base. Instrumentation was set up to monitor the base for sliding.

In the case of bare frames, the steel reinforcement for the columns was developed by embedding the steel cage into the footing beam before its casting. After the footing pad, columns were cast followed by the beam. The bare frame was constructed with the same dimensions of columns and beams as confining elements in the case of confined masonry to produce similarity in geometry for the purpose of comparison of both structures.

The construction of confined masonry walls was similar to the bare frames except for dowels of tie-columns embedded into the footing beam. The masonry was then assembled using common clay bricks measuring 225 mm × 113 mm × 75 mm (length × width × height) with 10 mm thick bed and head mortar joints. To improve the bond efficiency at the brick-mortar interface, all bricks were soaked as dry bricks have high water absorption. Half brick toothing was used on alternate brick courses during brickwork to ensure the masonry units were tightly packed with confining elements. The walls were built up to their full height in three stages with an English running bond, keeping the frog of bricks facing upwards to establish a strong interface. All bed and head joints between bricks were properly filled with mortar. After the masonry was constructed, tie-columns and a tie-beam measuring 225 mm × 113 mm and 113 mm × 225 mm (width × depth), respectively, were cast to fully confine the wall. All confining elements had four No. 3 deformed longitudinal steel bars and No. 2 transverse reinforcement. The thickness of the confining elements matched that of the masonry wall, which was 113 mm.

To measure the strain of longitudinal and transversal steel bars at critical sections of the columns, strain gauges were glued with cyanoacrylate adhesive. Steel strain gauges were also installed at critical sections of the beams to examine the strain of steel bars during loading before casting. The slump for the tie-columns was kept a little bit high at approximately 110 mm to allow easy flow of concrete into tooth gaps.

The OPC test specimens were water-cured for 28 days to ensure maximum shear strength, whereas GPC test specimens were subjected to ambient curing. The prototype test specimens' reinforcement details and geometric properties are shown in Figure 1.

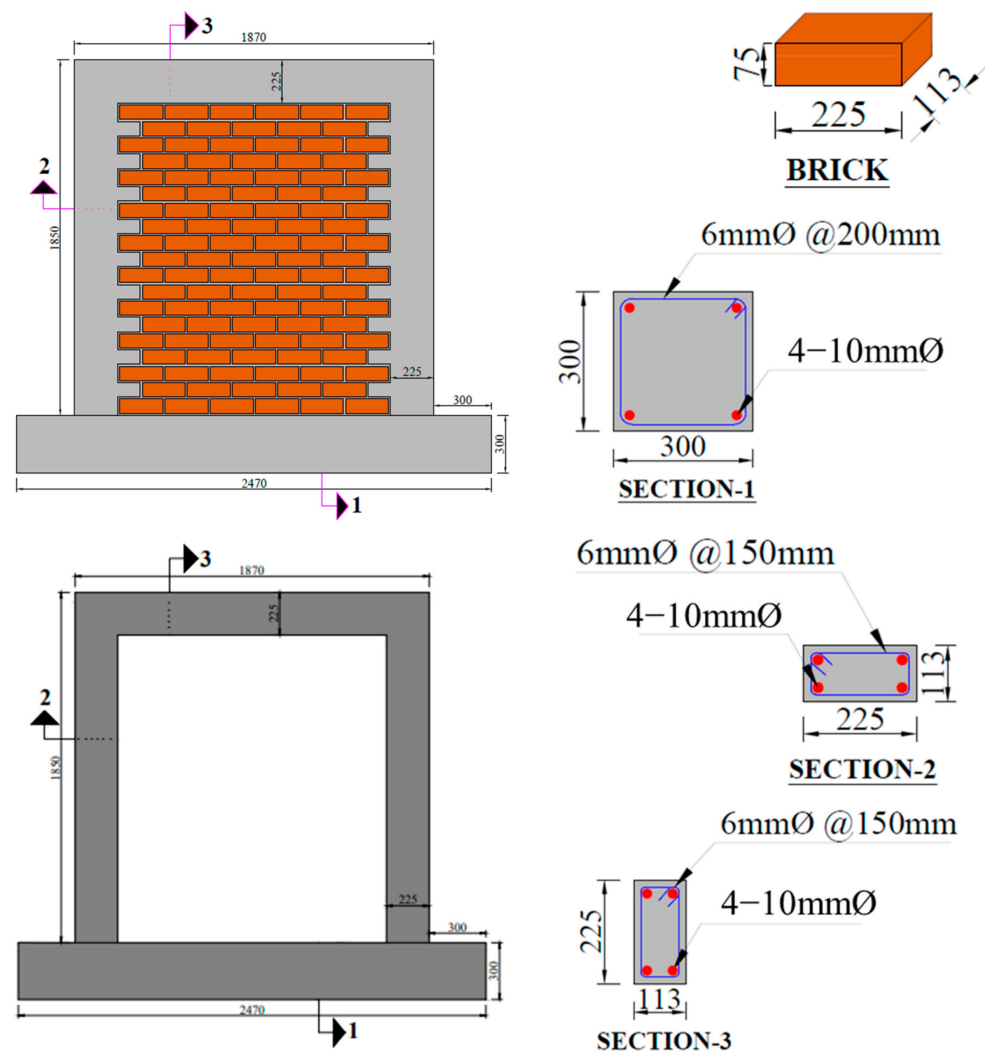


**Figure 1.** Schematics and reinforcement detailing of bare frame and confined masonry wall.

### 2.1.2. Materials and Properties

The material behavior of both types of concrete and mortar used in the construction of bare frames and confined masonry panels were determined through experimental testing according to the standards, given in Table 1. Margalla crush was used as coarse aggregate having a particle size ranging from 10 mm to 20 mm with an average size of 12.5 mm. The apparent specific gravity of coarse aggregates was determined as 2.66 g/cm<sup>3</sup> and the water absorption was 1.34% obtained by ASTM C127 [76]. The chemical composition of fly ash is listed in Table 2. The mix proportions used for conventional concrete and cement mortar were 1:2:4 with  $w/c$  0.45 and 1:3 (cement: sand) with  $w/c$  0.6, respectively, whereas the mix design of fly-ash-based geopolymer concrete was taken from past studies based on the optimal mechanical performance [77] and is given in Table 3. The same mix proportion of geopolymer mortar was adopted as in the case of cement mortar, with cement

replaced by fly ash along with alkaline activator solution provided in Table 3. The chemical solution used as a composite activator consisted of liquid sodium silicate ( $\text{Na}_2\text{SiO}_3$ ), and a 14-molarity solution of NaOH flakes. In both types of concrete and mortar, Lawrencepur sand was used, with a fineness modulus of 2.6, determined experimentally conforming to ASTM C136 [78]. Mortar cubes of 50 mm size were tested to obtain the compressive strength of the mortar. For the purpose of concrete, Sargodha crush was used with a particle size of 5–20 mm. The compressive strength of the masonry was determined by testing a four-brick stacked prism, whereas its modulus of elasticity was estimated by the gradient of the secant joining 5% to 33% on the compressive strength graph.

**Table 1.** Experimental material characteristics.

Properties	Material	Average Value (MPa)	Reference Standards
Compressive Strength, Elastic Modulus	Brick	$f_b = 19.74$ [COV 7.4%]	[79]
	Cement Mortar	$f_{jc} = 21.97$ [COV 6.5%]	[80]
	Geopolymer Mortar	$f_{jg} = 22.09$ [COV 7.1%]	
	Masonry (with cement mortar)	$f_m = 9.81$ [COV 8.5%] $E_m = 4700$	[81]
	Masonry (with geopolymer mortar)	$f_{mg} = 9.78$ [COV 4.9%] $E_{mg} = 4691$	
	Yield Strength	OPC Concrete	$f_{c'} = 31.37$ [COV 4.4%] $E_c = 24794$
GPC Concrete		$f_{cg'} = 32.96$ [COV 7.2%] $E_{cg} = 25102$	
Yield Strength	Steel Rebar (6 $\phi$ )	$f_y = 483$ [COV 2.1%] $E = 188671$	[84]
	Steel Rebar (10 $\phi$ )	$f_y = 537$ [COV 1.3%] $E = 191103$	

**Table 2.** Chemical composition of fly ash.

Category	CaO %	MgO %	SiO <sub>2</sub> %	SO <sub>3</sub> %	Al <sub>2</sub> O <sub>3</sub> %	Fe <sub>2</sub> O <sub>3</sub> %	L.O.I *
FA	7.6	2.1	79.92	0.35	3.22	2.31	3.1

\* Loss of ignition.

**Table 3.** Mix proportions of geopolymer concrete and mortar.

Material	FA (kg/m <sup>3</sup> )	Coarse Agg. (kg/m <sup>3</sup> )	Fine Agg. (kg/m <sup>3</sup> )	NaOH Solution (kg/m <sup>3</sup> )	NaOH (M)	Na <sub>2</sub> SiO <sub>3</sub> Solution (kg/m <sup>3</sup> )	Na <sub>2</sub> SiO <sub>3</sub> /NaOH	AA/FA	Water (kg/m <sup>3</sup> )
Concrete	368	1294	554	73.6	14	110.4	1.5	0.5	36.8
Mortar	368	-	1104	73.6	14	110.4	1.5	0.5	36.8

### 2.1.3. Instrumentation and Test Procedure

The experimental study was conducted in the Test Floor Laboratory of the UET Lahore. A total of two bare frames and two confined masonry walls were tested using the test set-up shown in Figure 2. Each of the bare frame and confined masonry walls was constructed with conventional concrete and geopolymer concrete on a robust RC footing beam with a cross-section of 300 mm × 300 mm, featuring an extended length of 300 mm on each side of the specimen to securely anchor it to the test floor. During the test, five LVDTs were used to record lateral, diagonal, and out-of-plane displacement as shown in Figure 2.

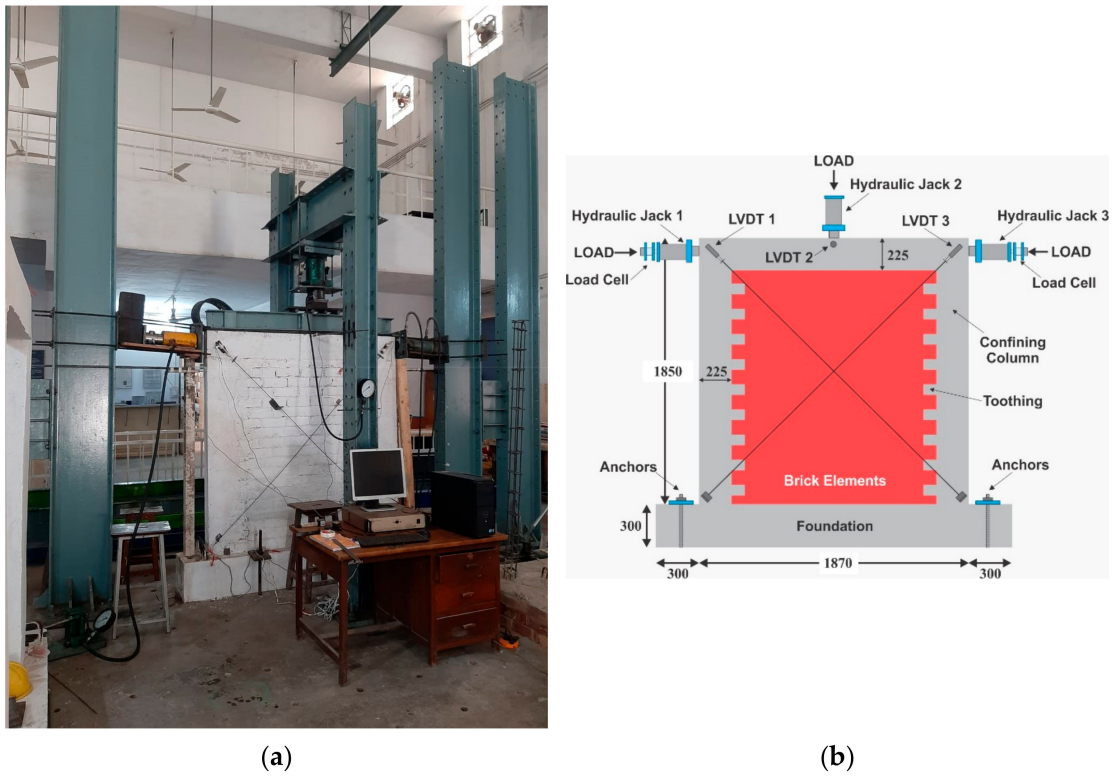


Figure 2. Experimental test setup (a) Actual, (b) Schematic.

A uniformly distributed gravity load was applied to the wall through a steel girder to simulate service roof load and was kept constant throughout the test. To allow for free lateral displacement during loading, four 50 mm diameter rollers were placed above the steel girder. Quasi-static in-plane reverse cyclic loading was then applied at the top of the beam-column joint with a low frequency of approximately 0.02 Hz, using hydraulic jacks on each side of the wall. Load cells were used to record lateral loads, and the lateral loading was increased incrementally by 5 mm after each cycle until failure, as per ACI 374.1-05 (ACI 374.1-05, 2014), as shown in Figure 3. The test was terminated when the specimens stopped taking further load and the strength degradation began together with considerable widening of bed joint cracks.

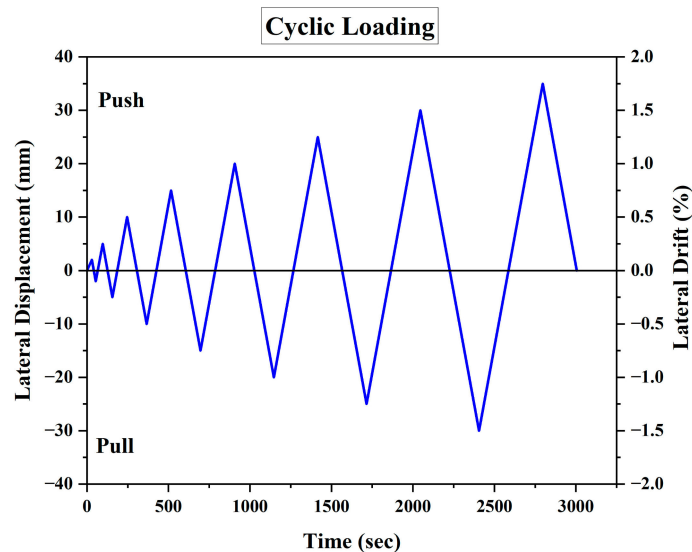


Figure 3. Quasi-static cyclic displacement time history.

## 2.2. Numerical Simulation

A numerical analysis was conducted to develop a three-dimensional finite element model of the confined masonry walls tested experimentally in the present study. The analysis utilized commercially available finite element software, ANSYS, which had been employed in earlier studies on masonry walls [85–89].

Based on past studies, there are various techniques utilized to analyze the structural response of masonry walls numerically. These techniques depend upon how accurately the model is capable of predicting the failure mechanisms. These techniques are categorized as detailed micro modeling, macro modeling, and simplified micro modeling.

The detailed micro modeling technique is very useful when most failure mechanisms are required to be analyzed. In this method, the mortar and bricks are considered continuum elements with defined failure criteria. The bricks and mortar interface are modeled with distinct elements representing discontinuities. Since, each part of the masonry, i.e., brick, mortar, and their interface, are modeled separately with their individual characteristics, therefore, this numerical approach takes more time to process the data. In contrast to the micro modeling technique, in the macro modeling approach the whole masonry panel is considered as a homogeneous element, where mesh size is the same as that of brick and the characteristics are assigned to a wall panel in place of mortar and brick separately. This modeling method is used due to the requirement for shorter data-processing time, but simultaneously, it is comparatively less accurate. Therefore, where more accuracy is not a big concern, this technique can be utilized, for example, for larger structures. However, in the simplified micro modeling, the general geometry of the wall including bricks is maintained, as in the detailed micro modeling, but the mortar joints and interface elements are modeled as discrete elements to represent a contact area. The compressive and shear stress properties are assigned to the mortar with the help of spring elements, and for the brick-mortar bond contact elements are used. This modeling technique requires less time for data processing as compared to the detailed micro-modeling approach. Based on the recommendations of previous research, a simplified micro-modeling technique was used in this study [90–95].

Reinforced concrete and brick units were modeled using three-dimensional hexahedron elements with eight nodes and three degrees of freedom at each node, with translational displacement along nodal  $x$ ,  $y$ , and  $z$  dimensions, in ANSYS [95]. The SOLID65 element is capable of crushing in compression and cracking in tension and can incorporate reinforcement rebar that is smeared throughout the reinforced concrete element. To model the steel rebar, the LINK180 element, which is a uniaxial tension-compression element with three degrees of freedom at each node, was used. The mortar joint was modeled using two nonlinear spring elements (COMBIN39) in parallel and one contact element (CONTA178) in series with the spring elements (Figure 4).

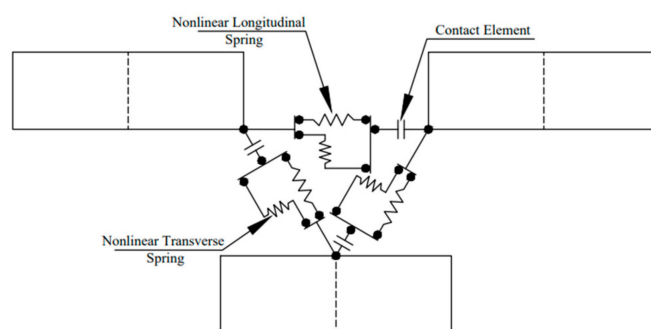


**Figure 4.** Brick-mortar joint detail.

The nonlinear springs represent the shear and axial response of the mortar, while the contact element represents the bond between the mortar and brick and considers friction as well. The properties of the spring and contact elements were determined directly from the

materials, with the force-deflection curve defined from the stress-strain curve. The force was defined by multiplying the stress by the tributary area over the node (Figure 5), and the deflection was expressed as the strain multiplied by the length of the spring, which was set to be 9/10 of the joint thickness, while the length of the contact element was 1/10 of the joint thickness.

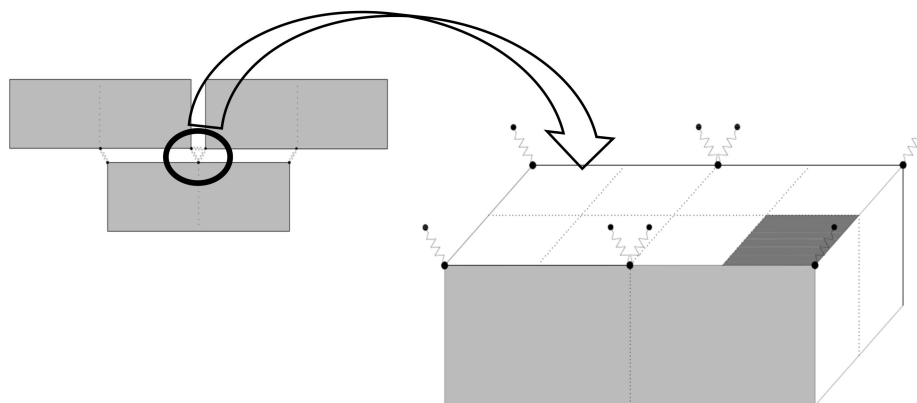


**Figure 5.** Tributary area on nodes for nonlinear springs.

The brick elements were meshed by dividing them vertically into two equal parts to connect them with adjacent upper and lower courses (Figure 5). The nodes of two bricks were connected with two spring elements in parallel and one contact element in series to model the mortar joint and the bond between brick and mortar, respectively. The two spring elements were assigned properties to express the longitudinal and transversal response of the mortar, while contact elements were assigned properties associated with the mortar and also friction to represent the bond between the brick and mortar. The confining elements of the wall were also modeled using SOLID65, and the steel rebar was embedded into the concrete using the LINK180 element. Before solving the analysis, all nodes of the wall were restrained along the z-direction to prevent out-of-plane movement of the panel. The lower nodes of the bottom course were restrained along all dimensions to provide fixed support at the bottom.

### 3. Results and Discussions

#### 3.1. Experimental Program

##### 3.1.1. Material Behavior

The material behavior of both types of concrete, mortar, and masonry wallets is illustrated in Table 1. Compressive strength is an important parameter to evaluate the structural performance of concrete. GPC typically has higher compressive strength compared to conventional concrete due to the strong chemical bonding between the binder and the aggregate. Additionally, geopolymer concrete often contains a higher proportion of fine aggregates, which contributes to the development of a dense and homogeneous microstructure. However, it is worth noting that the compressive strength of both kinds of concrete can be influenced by various factors such as mix design, curing conditions, water-to-binder ratio, and the size and type of aggregate. Therefore, a direct comparison of compressive strengths of two types of concrete in this study shows 4.94% more strength for geopolymer concrete. Past studies also endorse the higher compressive strength of geopolymer concrete compared to traditional concrete. For example, Neupane et al. [96] carried out a detailed study on the compressive strength of geopolymer and traditional concrete having different grades (40, 50, 65, and 80 MPa). With standard room-temperature curing of all specimens, it was observed that the compressive strength gain of geopolymer concrete was comparatively lower than conventional concrete at an early age; however, it was significantly higher at a later age. Reddy et al. conducted an experimental comparison of the compressive strengths of a novel steel-fiber-reinforced geopolymer concrete with

conventional concrete. The study found that the steel-fiber-reinforced geopolymer concrete had 13.4% higher compressive strength compared to the OPC concrete [97]. Moreover, the geopolymer mortar carries more compressive strength than OPC paste, as experimentally studied by Razak et al. [98]. It was concluded that the fly-ash-based geopolymer paste possesses more resistance to aggressive environments and compressive strength than OPC.

The second most important characteristic of a material contributing towards resistance to the applied load, Young's modulus of elasticity, also known as elastic modulus, is a measure of a material's stiffness and its resistance to deformation under load. In general, fly-ash-based geopolymer concrete has a higher Young's modulus of elasticity compared to conventional concrete. This indicates that fly-ash-based geopolymer concrete is stiffer and stronger than conventional concrete. However, the exact value of Young's modulus of elasticity of these materials can vary based on the specific mixture proportions and curing conditions used. The present study illustrates a 1.23% greater modulus of elasticity of geopolymer concrete compared to that of conventional concrete. In the literature, a large variety of experimentally-determined values of modulus of elasticity has been found for geopolymer concrete ranging from 30% lower to 20% higher than that of OPC. Bondar et al. [99] investigated the engineering properties of concrete made with alkali-activated natural pozzolan. The comparison of geopolymer concrete with traditional Portland cement concrete resulted in alkali-activated GPC possessing 5% to 20% higher modulus of elasticity after 14 days of ambient curing, making it a promising alternative to traditional concrete. However, Olivia et al. [100] experimentally evaluated a total of nine mixture variations by considering the impact of the ratio of sodium silicate to sodium hydroxide, the ratio of alkaline solution to fly ash, aggregate content, and curing method. The findings reveal that the modulus of elasticity of geopolymer concrete was 14.9–28.8% lower compared to ordinary Portland cement concrete. This suggests that a high content of silicate might enhance the elasticity of geopolymer concrete. Nath et al. [101] investigated eleven geopolymer specimens of different mix designs and two OPC cylinders to evaluate the modulus of elasticity at 28 and 90 days of ambient curing. The geopolymer concrete of similar grade to the OPC concrete achieved about 25–30% less modulus of elasticity than that of OPC at the age of 28 days, whereas at the age of 90 days' ambient curing, GPC could achieve modulus of elasticity in the range of 21.6% to 31.1% less than the value of conventional concrete. In view of the material behavior examined in the present research and previous studies, most of the findings endorse the superiority of alkali-activated fly-ash-based geopolymer concrete to ordinary concrete, which demonstrates the potential for developing and utilizing this alternative to traditional Portland cement concrete.

### 3.1.2. Hysteretic Response

The load-deflection hysteretic behavior of OPC-BF is given in Figure 6. During the early stages of loading and unloading, the hysteresis curves were nearly linear. As the lateral loading displacement increased, the specimen gradually entered an elastoplastic state, and its stiffness steadily declined due to the concentration of cracks at the columns and the beam-column joint. The flexural cracks initiated at the beam-column joint, at which, severe distress was noticed at increased load. In the later stages, more flexural cracks were produced at the column cross-section. The frame responded with almost symmetrical hysteresis loops by a difference of 7.8% between the peak positive and negative loads in the last cycle. The seismic resistance of the frame was discovered to escalate with each hysteresis, reaching a high of 25.39 kN and then declining to 22.81 kN during the final pushover, which corresponded to drifts of 2.30% and 3.16%, respectively. In the last cycles of load, the cracks started widening at the beam-column joint. It is important to note that the strength degradation of the bare frame was caused by plastic damage in the beam-column joints and column cross-section. A sudden decrease in seismic strength was noticed in the frame after reaching the maximum drift value, leading to the termination of the test. On the whole, the hysteretic curve of the specimen was pinched at higher drift levels. Additionally, the drift level at the peak load ( $\delta_m$ ) of the conventional concrete bare frame

was calculated to be 3.16% during push and 0.93% during pull cycles. The initial stiffness ( $K_{C0}$ ) was recorded as 8.47 kN/mm.

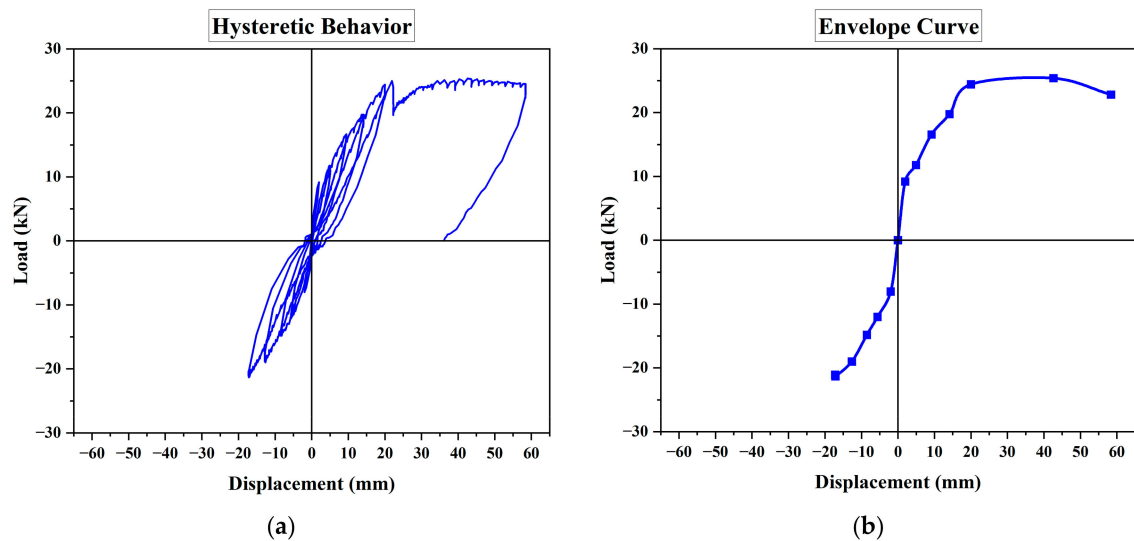


**Figure 6.** Experimental results of OPC-BF (a) Hysteretic response (b) Envelope curve.

The lateral load-displacement curve of GPC-BF is displayed in Figure 7. Initially, the specimen was in the elastic phase, with the load-deflection curve exhibiting a linear relationship. As lateral drift increased, cracks appeared near the beam joint, causing the hysteresis curve to slightly bend and display nonlinear behavior. This indicated that the specimen had entered the elastoplastic phase, with the enveloping area of the hysteresis loop increasing. The last push and pull load exhibiting peak positive and negative values of lateral load carrying capacity of the frame showed almost no difference. During the inelastic phase, the lateral load of the specimen gradually increased in each cyclic load, reaching a maximum value of 25.51 kN in the last pushover and gradually decreasing to 24.90 kN corresponding to 3.13% and 3.19%, respectively. Up to 58.9 mm lateral displacement, the geopolymer concrete frame resisted maximum loads. By further escalating the lateral displacements, large cracks were developed in the beam-column joint, due to which lateral load-carrying capacity decreased suddenly signaling the termination of the test. From the figure, it can be seen that the hysteresis loops are narrow at the beginning and wider at the end of the displacement cycles. This indicates that, at lower lateral displacements, crack widths were smaller, and less energy was dissipated. However, as lateral displacement increased, crack widths also increased, leading to greater energy dissipation. GPC-BF illustrated a good and stable hysteresis behavior with a slight pinching effect. The drift level at the peak load ( $\delta_m$ ) of the geopolymer concrete bare frame was estimated to be 3.19% during push and 1.34% during pull cycles. The initial stiffness ( $K_{C0}$ ) was recorded as 8.77 kN/mm.

Approximately, all the seismic characteristics of the conventional concrete bare frame and alkali-activated fly-ash-based geopolymer concrete have shown good concordance with each other. The GPC frame has exhibited better lateral properties than the traditional concrete frame. The initial stiffness of the GPC frame has been observed 3.5% more than that of the OPC frame. However, the initial stiffness of the two frames has been found very close to the past studies [102–104]. Similarly, the ultimate positive and negative load of the GPC frame has been estimated 0.47% and 4.4%, respectively, higher than that of the cement concrete frame. The maximum lateral load strength of the OPC-BF and GPC-BF were found to be 1.37 and 1.54 times the cracking load.

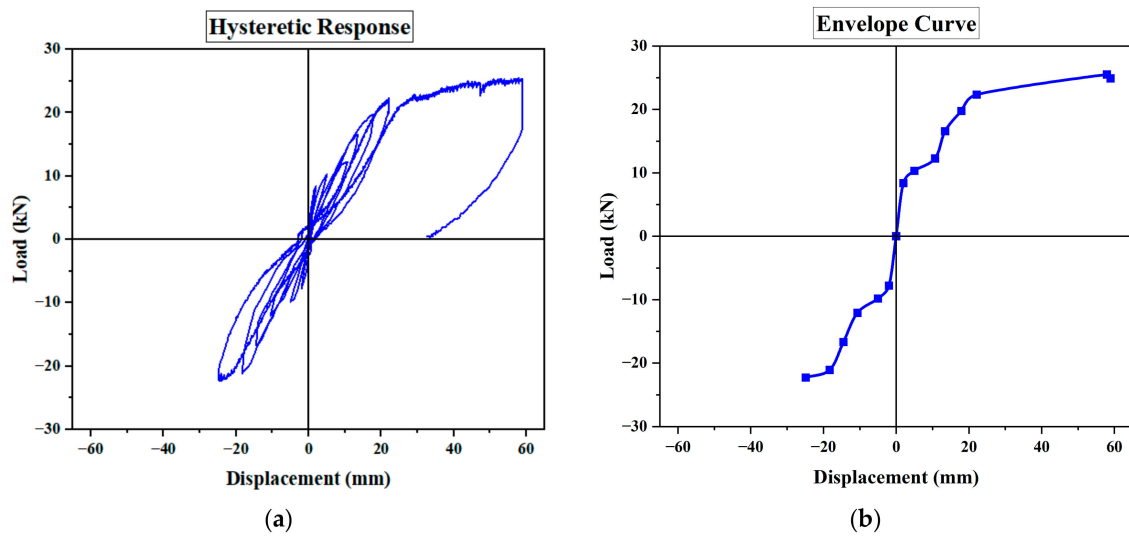
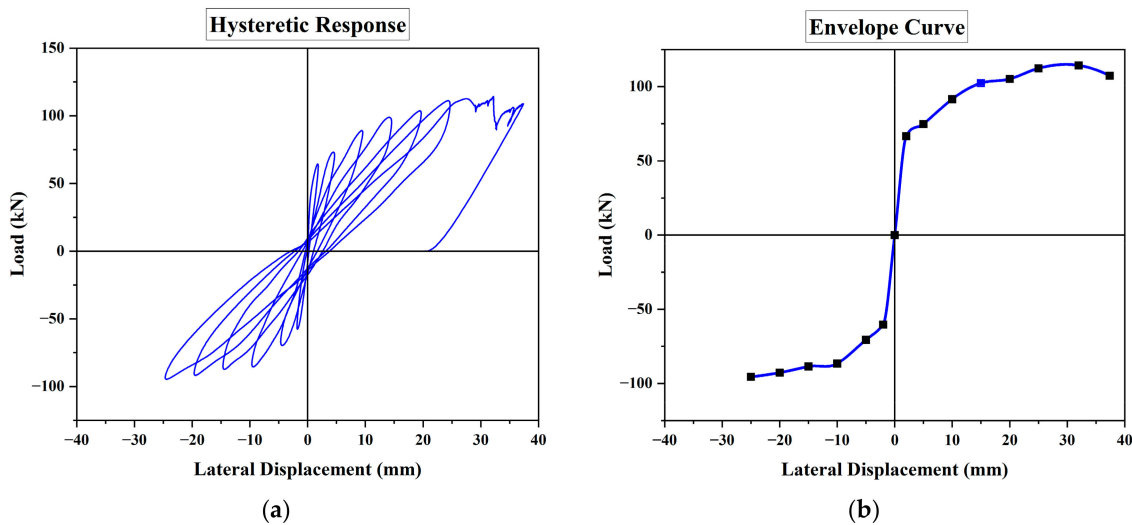


Figure 7. Experimental results of GPC-BF (a) Hysteretic response (b) Envelope curve.

The results of OPC-BF and GPC-BF show good match with the past studies. The study conducted by Sumajouw et al. [105] investigated the performance of slender columns made of fly ash concrete (measuring 175 mm × 175 mm × 1500 mm) when subjected to axial compression and uniaxial bending. The research focused on several key parameters, including compressive strength (40 MPa and 60 MPa), longitudinal reinforcement ratio (1.47 and 2.95), and load eccentricity (15, 35, and 50 mm). The study revealed that columns made of fly ash geopolymer concrete demonstrated behavior similar to that of ordinary Portland cement (OPC) concrete. Consequently, the existing design provisions contained in current standards and codes can be employed to design reinforced fly-ash-based geopolymer concrete columns.

Similarly, Rahman et al. [106] conducted a study on twelve slender columns made of fly ash concrete (measuring 175 mm × 175 mm × 1500 mm) that were subjected to axial compression and different combinations of biaxial load eccentricities. The study focused on several key parameters, including compressive strength (ranging from 37 MPa to 63 MPa), longitudinal reinforcement ratio (1.47 and 2.95), load eccentricity in the x direction (15, 30, 35, 50, and 70 mm), and load eccentricity in the y direction (15, 30, 35, 50, and 70 mm). The results of their study demonstrated the potential for fly ash geopolymer concrete to be used in structural applications instead of conventional concrete structures.

The in-plane load vs. deformation of the conventional concrete tested specimen is shown in (Figure 8). The hysteretic response of the OPC-CM wall panel illustrated almost proportional cycles in pushing and pulling directions. The seismic strength of the wall specimen was found to increase in each hysteresis reaching a maximum value of 114.3 kN and then decreasing to 109.1 kN in the last push load corresponding to 1.73% and 2.02% drifts, respectively. After the peak drift value, a sudden drop in seismic strength was observed in the wall panel, which was the main reason for the test termination. The pinching behavior was witnessed during the seismic performance of the panel at a larger drift level because of confinement. The distribution of the lateral load along the cross-section of the masonry  $A_w$  caused the development of the shear stress in the masonry panel ( $V_{max}/A_w$ ), i.e., 0.67 MPa. Further, the drift level at peak load ( $\delta_m$ ) of the confined masonry wall was estimated as 1.73% at push and 1.35% during the pull cycles. The initial stiffness ( $K_{C0}$ ) was observed as 35 kN/mm.



**Figure 8.** Experimental results of OPC-CM (a) Hysteretic response (b) Envelope curve.

The hysteretic behavior of the GPC-CM test specimen exhibited slight irregular and asymmetric loops in the push and pull cyclic loads as shown in (Figure 9). The wall specimen showed almost symmetric loops until the onset of bed joint cracks in the second loop of lateral load, after which the structural behavior of the wall shifted to an elastoplastic state and the wall stiffness steadily degenerated owing to the development and concentration of more and more cracks in the masonry pier. As with the cement concrete wall, the GPC wall also showed increasing seismic load capacity in each cycle reaching a maximum value of 119.10 kN at the drift of 2.32% in the last push load, after which the wall stopped taking further load and the lateral load carrying capacity of GPC-CM started decreasing and a sudden drop in lateral strength was observed, at which point the test was terminated to avoid any accident or damage to the equipment attached to the wall. The initial stiffness ( $K_{C0}$ ) and the development of the shear stress in the masonry pier ( $V_{max}/A_w$ ) were estimated as 55.45 kN/mm and 0.66 MPa, respectively.

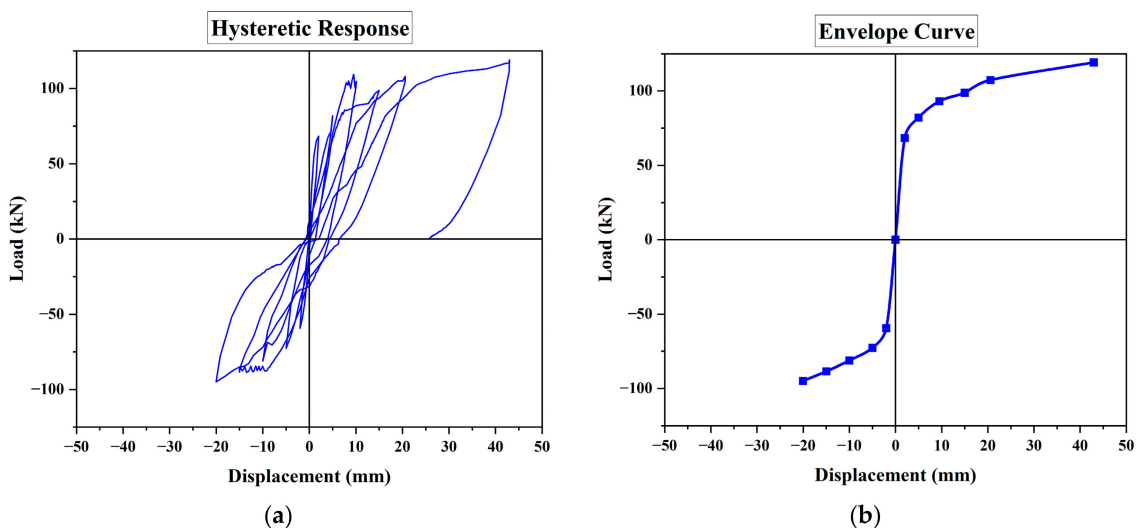


**Figure 9.** Experimental results of GPC-CM (a) Hysteretic response (b) Envelope curve.

As with bare frame structures, GPC confined masonry has also shown a good match of seismic characteristics with the traditional concrete wall. The initial stiffness of the GPC wall specimen was estimated 45.2% higher than that of OPC wall masonry, whereas wall shear stress was calculated as 1.5% greater in OPC-CM. As far as peak lateral load is concerned,

GPC confined masonry has exhibited a 4.11% greater peak lateral load than the OPC wall. The higher seismic capacity of alkali-activated fly-ash-based geopolymer concrete confined masonry is certainly due to more compressive strength and Young's modulus of elasticity of geopolymer concrete as determined experimentally in the present study. Approximately similar behavior is also evident from the previous research as discussed in the material behavior section. The backbone curves of both walls were plotted by joining the peak resistance of the adjacent displacement cycles (Figures 8 and 9). The maximum lateral load-bearing capacity of the OPC-CM and GPC-CM were found to be 1.52 and 1.66 times the cracking load, which are slightly more than the squat wall tested by Borah et al. [107].

The maximum seismic strength ( $V_{max}$ ) of all the specimens determined experimentally and the corresponding drift ( $\delta_m$ ) are presented in Table 4. The cyclic stiffness ( $K_c$ ) was calculated for the first hysteresis loop at every drift level as the gradient of the line connecting the maximum points of positive and negative curves. The stiffness degradation ( $K_c/K_{c0}$ ) at each drift level was drawn concerning the drift  $\delta$  normalized with regard to the drift level in the first loading cycle,  $\delta_0$  (Figure 10a). The strength variation factor ( $C_{sv} = V/V_{max}$ ) obtained from the normalization of seismic loads determined against various drift points with  $V_{max}$  was plotted against  $\delta/\delta_m$  (Figure 10b). The plot shows that the increment in strength was found in the specimen due to confining elements in the wall.

Table 4. Hysteretic response of test walls.

Specimen	$V_{cr}$ (kN)	$V_{max}$ (kN)			$V_{max}/A_w$ (MPa)	$\delta_m$ (%)			$\mu_d$
		Push	Pull	Avg		Push	Pull	Avg	
OPC-BF	18.52	25.39	21.34	23.36	-	3.15	0.93	2.04	1.29
GPC-BF	16.56	25.51	22.30	23.90	-	3.19	1.34	2.26	1.02
OPC-CM	75.7	114.3	98.2	106.2	0.67	2.02	1.35	1.68	15.42
GPC-CM	51.14	85.10	58.25	71.67	0.44	2.32	1.08	1.70	3.27

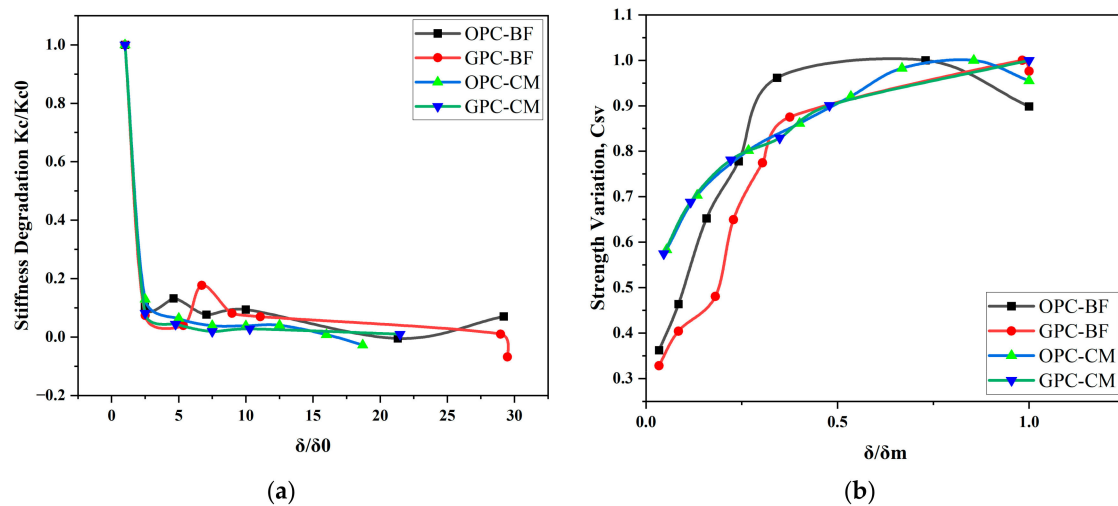
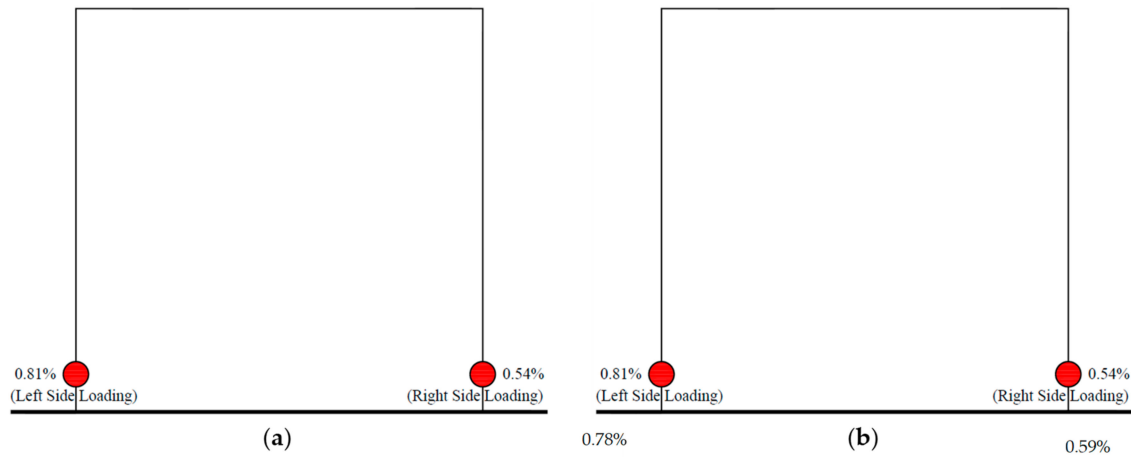


Figure 10. (a) Stiffness degradation (b) Strength variation.

### 3.1.3. Strain in Longitudinal Reinforcement

The strain in longitudinal reinforcement was determined at the most critical sections of the tie-columns, where plastic hinges were expected to develop, to evaluate the nonlinearity of the structures, with the help of a data logger. The strain gauges installed at the bottom of each tie-column recorded large strains related to the yielding of longitudinal reinforcement. The lowest values of the lateral drift level with respect to the yielding of the reinforcement rebars are shown in Figure 11. The drifts corresponding to the yielding of steel rebars in all test specimens were observed to be approximately comparable to each other due to the fact that the same steel was used in all specimens. It is pertinent to mention that the

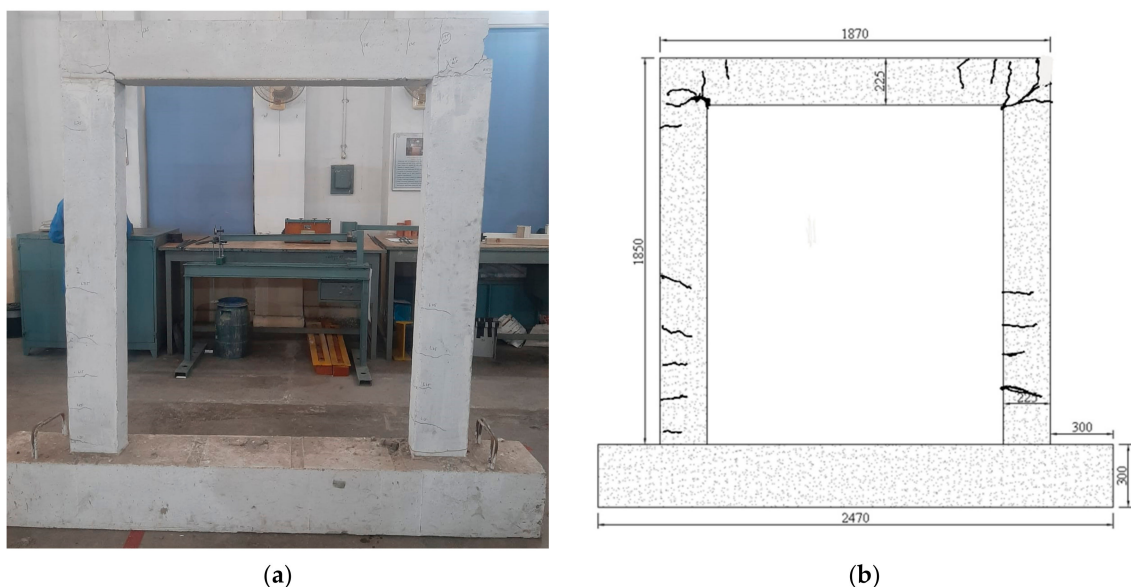
yielding phenomenon in steel rebars is the same regardless of the type of concrete used in a structure, therefore the occurrence of close values of drift level related to the steel yielding is certain.



**Figure 11.** Locations of reinforcement yielding and corresponding drift values (a) OPC-CM (b) GPC-CM.

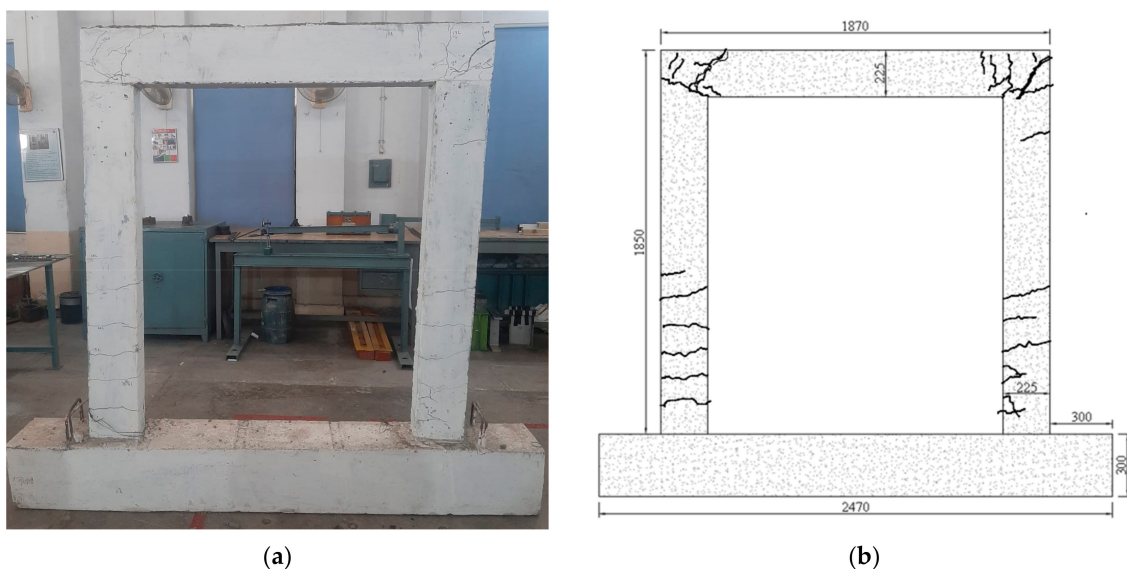
#### 3.1.4. Failure Mechanism

Figure 12 displays the cracking pattern of OPC-BF, denoting the ordinary Portland cement bare frame. In the OPC-BF specimen, the initial crack appeared at the beam-column joint at 18.52 kN push load corresponding to the drift level of 0.67%. On further displacement in the pulling direction, the first flexural crack appeared at the column cross-section near the bottom, against the lateral load 19.7 kN at 0.76% drift. Few flexural cracks appeared to spread on both column cross sections at increased lateral load. At the end of the last pushover, shear cracks at the beam-column joint and a flexural crack at the bottom of the right column widened and propagated. The frame specimen achieved maximum seismic strength as 25.39 kN and 21.34 kN in the push and pull cyclic loads against the drift levels of 3.15% and 0.93% respectively. The maximum lateral displacement noted in the test specimen was 58.4 mm in the last pushover. The beam-column joint shear crack width was measured as 37 mm, whereas the maximum width of the flexural crack at the bottom of the column was recorded as 11 mm.



**Figure 12.** Crack pattern of OPC-BF (a) failure pattern of actual sample, (b) crack pattern diagram.

The fly-ash-based geopolymer concrete bare frame, denoted as GPC-BF, exhibited a ductile behavior and plastic hinges were fully produced at the beam-column joints and bottom of the columns as shown in Figure 13. The first crack appeared near the beam joint at the lateral load of 16.56 kN at 0.72% drift. Further, an increase in load to 19.75 kN against 0.97% lateral drift caused the appearance of flexural cracks in the columns. These flexural cracks were produced mostly near the bottom of columns. The most vulnerable places to failure in a bare frame are usually the bottom of columns and beam-column joints. At the lateral load of 22.32 kN push cycle corresponding to the drift level of 1.2%, the shear cracks at the beam-column joint widened significantly. The maximum lateral strength achieved by the geopolymer concrete frame specimen were 25.51 kN and 22.3 kN corresponding to the 3.18% and 1.34% drifts in the push and pull load cycle, respectively. The ultimate lateral displacement attained by the specimen was recorded as 58.9 mm in the final pushover. The maximum flexural crack width near the bottom of columns and shear crack width at the beam-column joint were measured as 10 mm and 29 mm, respectively. Both the test specimens have shown very similar failure modes and crack patterns with a slightly smaller crack width in the case of GPC-BF.



**Figure 13.** Crack pattern of GPC-BF (a) failure pattern of actual sample, (b) crack pattern diagram.

The specimen OPC-CM, denoting a confined masonry wall panel made of ordinary Portland cement concrete, was dominated by the shear failure of confining elements and crisscross mortar joints (Figure 14). At a drift level of 0.22%, corresponding to a lateral load of 75.74 kN for the pushing direction, the first crack initiated at the bed joint of mortar near the top. On further increasing lateral load, the cracks started propagating downward through the bricks-mortar joints at 0.54% drift against 89.85 kN. Diagonal stair-stepped cracks spread from the column-beam joint to the bottom of the other column through the bricks interface at 1.08% drift and a lateral load of 103.21 kN. On increasing further lateral drift, flexural cracks appeared in one tie-column. The possible reason for flexural cracks is the rocking of the masonry panel after the reinforced tie-column approaches the maximum tension capacity at the base. Most of the diagonal cracks developed passed through the mortar joints and only a few went through the bricks. The wall specimen achieved maximum lateral load-bearing capacity in pushing and pulling direction as 114.29 kN and 108.48 kN against drift levels of 1.73% and 1.35%, respectively. The peak lateral displacement recorded in the test specimen was approximately 37.4 mm in the last pushing direction. The diagonal crack width was measured as 24 mm, whereas the largest width of flexural cracks in tie-column was noted as 9.0 mm. The damage in the specimen was mostly concentrated in the top one-third part.

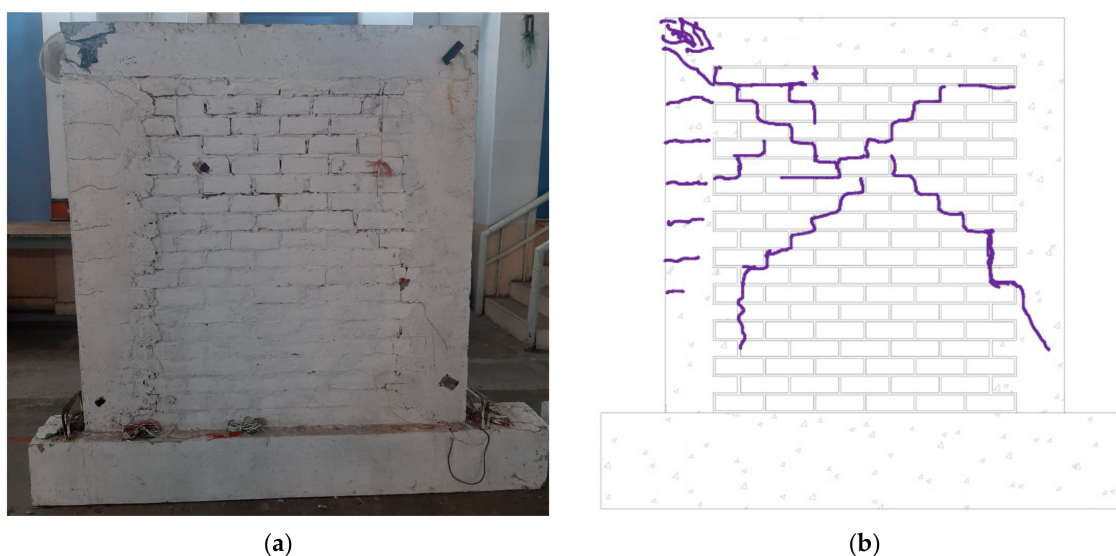


**Figure 14.** Crack pattern of OPC-CM (a) failure pattern of actual sample, (b) crack pattern diagram.

The failure mode in the GPC-CM wall, designating GPC confined masonry, may be characterized by the shear failure of masonry as well as confining elements including the tie-beam (Figure 15). The very first crack developed at the bed joint of bricks near the top left of the masonry close to the tie-column at 0.25% drift and 71.73 kN lateral load in the pushing direction. On increase in load, until 86.50 kN corresponding to 0.49% drift, the cracks' dissemination started downward along the bed and head joints. The first crack developed, spread upward, and entered the tie-column against 0.81% drift and 98.75 kN lateral load. The diagonal crisscross cracks produced propagated upward into the tie-column and downward into masonry. At 1.08% drift and 94.95 kN seismic load in the pulling direction, the right column-beam joint failed badly with considerable crack size. Further increase in lateral displacement led to shear cracks in the tie-beam and flexural cracks in the left tie-column at 1.11% drift and 107.98 kN lateral load in the sixth cycle of load. At the same load, the mortar spalled off at the center of the masonry wall. Almost all the cracks passed through the brick interface due to weak brick-mortar joints. The crack distribution was observed uniformly across the test wall. The wall specimen exhibited peak load carrying capacity of 119.1 kN and 95.0 kN in pushing and pulling directions at 2.32% and 1.08% drifts, respectively. The ultimate lateral displacement noted was 42.97 mm in the last push. The maximum shear crack width measured in the test specimen was around 28 mm and the width of flexural cracks in the tie-column and shear cracks in the tie-beam were recorded as 8.0 mm and 4.0 mm, respectively.

In both walls, the failure mode may be considered as the shear failure in form of diagonal cracks in the masonry panel propagated in slanted directions. The failure mechanism and the damage pattern were very similar to the research conducted by El-Diasity et al. on confined masonry under cyclic load [108]. The existence of the confining elements prolonged the occurrence of shear cracks in the masonry panel [109]. It is pertinent to mention that no separation was noticed at the toothed interface between confining columns and the masonry panel, clearly illustrating a significant advantage of confined masonry over infilled masonry structures [110]. The test experiments were terminated at the stage when the collapse prevention (CP) level of wall performance was attained as mentioned in ASCE/SEI 41-06 [111].

The cracking load of OPC-CM was observed to be 5.44% greater than that of GPC-CM. In GPC-CM, almost all the cracks propagated through the masonry joints separating the mortar from the brick interface instead of the crack passing through the geopolymer mortar.

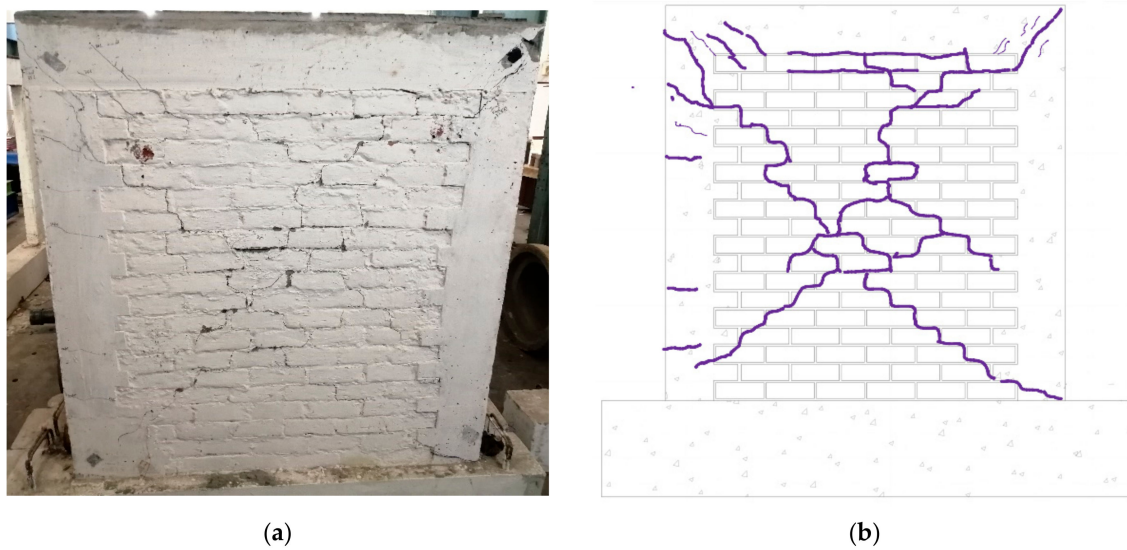


**Figure 15.** Crack pattern of GPC-CM (a) failure pattern of actual sample, (b) crack pattern diagram.

### 3.2. Numerical Modeling

The validation of the numerical model through experimental testing is considered a crucial aspect of FEA-based research to determine the accuracy of simulated parameters. Two confined masonry walls were tested experimentally to validate the numerical models used in this study. The wall panels built with confining elements of 225 mm depth and longitudinal reinforcement of No. 10 were tested under reverse cyclic loading. The seismic behavior of the test specimens was compared with that of the numerical models, which showed good agreement.

The comparison of the numerical model and experimental results of OPC-CM showed a difference of 10.81% in seismic capacity ( $V_{num}$ ) as shown in (Figure 16a). The numerical validation also revealed very similar hysteretic behavior in initial cycles, with increased energy dissipation at higher drift level. It is clear from the envelope curves that the numerical model demonstrated an increase in lateral strength with an increase in lateral drift, just as in the experimental results. The initial stiffness found from the numerical analysis was closely comparable with the experimental result by a difference of 5.4%.

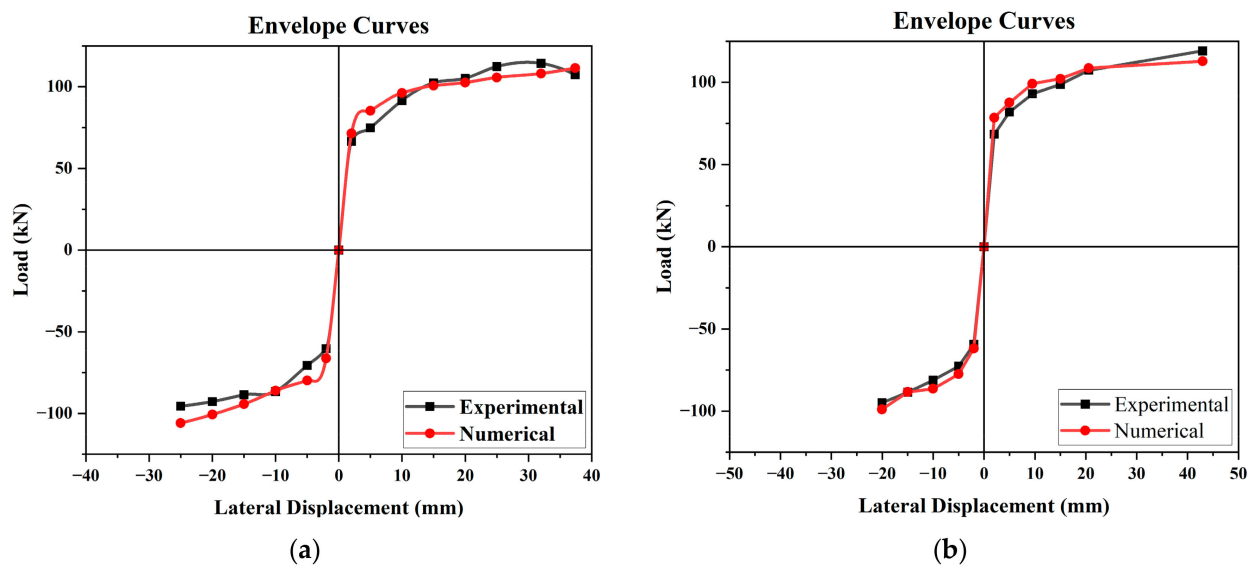


**Figure 16.** Comparison of experimental and numerical results (a) OPC-CM (b) GPC-CM.

Figure 16b illustrates the validation of the numerical model of GPC-CM by experimental results with a difference of 5.39% in peak lateral load. Similar to the OPC masonry case, FE analysis of the GPC wall also depicted an increasing trend of lateral load capacity with an increase in drift level as compared to the experimental results, evident from the backbone curves. The initial stiffness calculated from the numerical analysis was almost matchable to the experimental result by a difference of 6.1%.

Figure 17 displays the contour plot of both wall panels at the stage of failure. The diagonal contours that appeared on the damaged shape, clearly indicate that two panels failed in shear which matched with the failure mode of the tested walls. The FE model of conventional concrete confined masonry reached its maximum compressive strength and failed at the toe of the confining column, whereas the GPC model failed at the point of load application after reaching the peak compressive strength. The principal stresses varied as a result of loading and unloading during push and pull. The FE model, despite limitations in showing bed joint cracks, provided an approximate agreement with experimental damage as represented by stress contours in ANSYS (Figure 17).

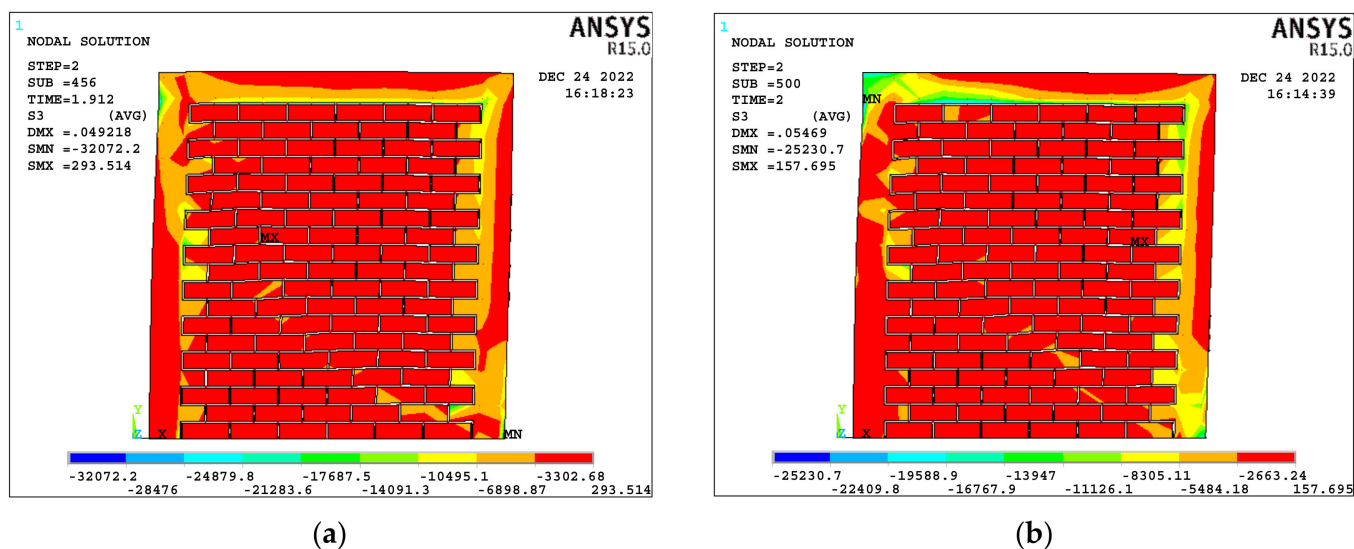


Figure 17. Contour plots of damaged shape (a) OPC-CM (b) GPC-CM.

#### 4. Comparison of Seismic Parameters

Geopolymer concrete confined masonry has shown considerable resistance to seismic load in this study. The lateral load strength of the GPC masonry wall has presented a good concordance not only with the conventional concrete confined masonry in this study. It is pertinent to mention that the lateral load-carrying capacity of confined masonry walls with an even higher reinforcement ratio has been observed to be less than that of a GPC wall. From Table 5, it is observed that GPC confined masonry has proved to be a seismically resistant structure in comparison to non-engineered masonry walls. The results exhibited comparable seismic resistance to other confined masonry tested in the past as given in Table 6. A comparison has also been drawn between the present study, especially regarding GPC confined masonry, and the past studies on infill masonry and bare frame in Tables 7 and 8, illustrating the significant advantages of GPC masonry over cement concrete infill masonry and bare frame.

**Table 5.** Comparison of the present study with past studies on unconfined masonry.

Sr. No	Study	Aspect Ratio (H/L)	$\rho$ (%)	Cracking Load $V_{cr}$ (kN)	Maximum Load $V_{max}$ (kN)	$V_{max}/V_{cr}$	Failure Mode
1	Ashraf [112]	1.08	-	-	77.8	-	Rocking
		1.08	-	-	103.1	-	Rocking
		1.08	-	47.0	120.3	2.55	Shear
		1.08	-	39.5	131.7	3.33	Shear
2	Nadège et al. [113]	1.22	-	-	12.0	-	Shear-Flexure
3	A Hasnat et al. [114]	0.75	-	4.42	13.1	2.96	Rocking
4	Konthesingha et al. [115]	1.0	-	-	257	-	Shear
		0.5	-	-	345	-	Rocking
5	Mojsilovic et al. [116]	1.0	-	-	89.17	-	Compression (Toe Crushing)
		1.0	-	-	145.89	-	Compression (Toe Crushing)
		1.0	-	-	53.37	-	Rocking
6	OPC-BF	0.99	1.08	18.52	25.39	1.37	Ductile
7	GPC-BF	0.99	1.08	16.56	25.51	1.54	Ductile
8	OPC-CM	0.99	1.08	75.7	114.3	1.51	Shear
9	GPC-CM	0.99	1.08	51.1	85.1	1.66	Shear

**Table 6.** Comparison of the present study with past studies on confined masonry.

Sr. No	Study	Aspect Ratio (H/L)	$\rho$ (%)	Cracking Load $V_{cr}$ (kN)	Maximum Load $V_{max}$ (kN)	$V_{max}/V_{cr}$	Failure Mode
1	Aguilar et al. [117]	1	1.51	103.1	140.6	1.36	Shear
2	Yáñez et al. [118]	0.61	1.12	68.5	127	1.85	Shear
		0.61	1.12	128.5	185.5	1.44	Shear
3	Marinili et al. [119]	0.77	2.25	142.2	205.9	1.45	Shear
4	Zabala et al. [120]	0.97	0.79	82.6	118	1.42	Shear
		0.97	2.01	140.76	207	1.47	Shear
5	Bourzam et al. [121]	1.62	2.01	70	81.4	1.16	Shear
6	Gavilan et al. [122]	1.52	2.82	71.3	75.8	1.06	Shear
		0.98	2.82	100.5	157.0	1.56	Shear
		0.67	2.82	250.2	320.8	1.28	Shear
7	Colunga et al. [123]	1.00	1.18	49.0	80.4	1.64	Shear
		1.63	0.72	34.1	47.5	1.39	Shear
8	Borah et al. [107]	1.30	0.72	38.2	55.8	1.46	Shear
		0.93	0.72	60.7	81.2	1.34	Shear
9	OPC-BF	0.99	1.08	18.52	25.39	1.37	Ductile
10	GPC-BF	0.99	1.08	16.56	25.51	1.54	Ductile
11	OPC-CM	0.99	1.08	75.7	114.3	1.51	Shear
12	GPC-CM	0.99	1.08	51.1	85.1	1.66	Shear

**Table 7.** Comparison of the present study with past studies on infill masonry.

Sr. No	Study	Aspect Ratio (H/L)	$\rho$ (%)	Cracking Load $V_{cr}$ (kN)	Maximum Load $V_{max}$ (kN)	$V_{max}/V_{cr}$	Failure Mode
1	Kuang et al. [124]	0.60	2.57	248	432	1.74	Shear
2	Ozkaynak et al. [125]	0.75	1.00	48.5	89.7	1.85	Shear
3	Van et al. [126]	0.61	1.57	13.7	36.6	2.67	Shear
		1.01	1.57	11.4	43.5	3.80	Shear
4	Li et al. [127]	0.74	1.09	-	261.1	-	Shear
		0.74	1.09	-	390	-	Shear
5	Durrani et al. [128]	0.97	1.76	33.3	49.7	1.49	Shear
6	OPC-BF	0.99	1.08	18.52	25.39	1.37	Ductile
7	GPC-BF	0.99	1.08	16.56	25.51	1.54	Ductile
8	OPC-CM	0.99	1.08	75.7	114.3	1.51	Shear
9	GPC-CM	0.99	1.08	51.1	85.1	1.66	Shear

**Table 8.** Comparison of the present study with past studies on bare frame.

Sr. No	Study	Aspect Ratio (H/L)	$\rho$ (%)	Cracking Load $V_{cr}$ (kN)	Maximum Load $V_{max}$ (kN)	$V_{max}/V_{cr}$	Failure Mode
1	Jiang et al. [129]	0.49	1.57	129.7	379.3	2.92	ductile
2	Peng et al. [130]	0.57	1.03	-	334.7	-	ductile
3	Ozkaynak et al. [125]	0.75	1.00	20.6	41.6	2.02	ductile
4	Van et al. [126]	1.01	1.57	7.8	22.7	2.9	ductile
5	Penava et al. [131]	0.68	2.35	61.2	106.4	1.74	ductile
6	OPC-BF	0.99	1.08	18.52	25.39	1.37	Ductile
7	GPC-BF	0.99	1.08	16.56	25.51	1.54	Ductile
8	OPC-CM	0.99	1.08	75.7	114.3	1.51	Shear
9	GPC-CM	0.99	1.08	51.1	85.1	1.66	Shear

## 5. Viability of Geopolymer Concrete

Geopolymer concrete is a type of concrete that is made using industrial waste materials such as fly ash, blast furnace slag, and other mineral admixtures instead of traditional cement. The resulting material is known to have several advantages over conventional concrete, including improved mechanical properties, increased durability, and reduced carbon emissions.

Recently, sustainable, strong and durable concrete has become an important aspect of the construction industry [132–135]. Geopolymer concrete is considered to be more environmentally friendly than conventional concrete because it reduces the need for Portland cement, which is a major contributor to carbon dioxide emissions during its manufacturing process. By using industrial waste materials such as fly ash in geopolymer concrete, it is possible to reduce the amount of waste that is sent to landfills while simultaneously producing a material that is strong and durable.

One of the key benefits of geopolymer concrete is its strength and durability. In this study, geopolymer concrete has shown higher compressive strength (3.89%) and Young's modulus of elasticity (1.23%) than traditional concrete, and the similar mechanical behavior of geopolymer concrete is evident from past studies [96–101]. These attributes make it a

promising material for a wide range of applications, including infrastructure projects such as bridges, highways, and buildings [105,106,132].

In this paper, the research to investigate the structural performance of geopolymer concrete bare frames against the seismic load has demonstrated 3.5% and 0.93% higher values of initial stiffness and maximum lateral load carrying capacity, respectively, of the GPC frame as compared to the OPC frame. The investigation was extended to the experimental and numerical study of confined masonry with comparable results. The findings highlight that GPC confined masonry has displayed 45.2% and 4.11% more initial stiffness and peak seismic strength, respectively, than traditional concrete walls.

The topmost benefit of geopolymer concrete is its low carbon footprint. The production of traditional Portland cement is responsible for a significant amount of carbon dioxide emissions, and the use of geopolymer concrete can significantly reduce these emissions. In addition, the use of industrial waste materials in geopolymer concrete can reduce the amount of waste that is sent to landfills, which can help to reduce environmental pollution.

Overall, geopolymer concrete shows promise as a viable and green substitute for conventional concrete. Its strength, durability, and low carbon footprint make it a promising material for a wide range of infrastructure projects. However, more research and development are needed to improve the production process and address the challenges associated with its use.

## 6. Conclusions

The aim of the research was to compare the performance of fly-ash-based geopolymer concrete bare frames and confined masonry wall panels with conventional OPC concrete. The study aimed to provide valuable insights into the design and evaluation of GPC confined masonry structures, especially in high seismic regions, to encourage cost-effective, eco-friendly, sustainable, and earthquake-resistant construction. The experimental and numerical program evaluated the seismic behavior of bare frames and single-wythe confined masonry walls made with geopolymer and conventional concrete, with an aspect ratio close to 1.0, subjected to displacement-controlled pseudo-static reverse cyclic loading. The response of the test specimens was analyzed based on seismic parameters, such as lateral load strength, initial stiffness and stiffness degradation, maximum drift level, failure mode, and damage pattern. Finite Element models of confined masonry walls were established using a simplified micro-modeling technique and validated based on the test results. The study compared the significant structural parameters of the walls tested in this study with those of unconfined masonry, confined masonry, infill masonry, and bare frame tested in previous research.

The research yielded several inferences drawn from both experimental and numerical analyses. Firstly, the mechanical strength parameters of the GPC and OPC concrete mixtures were compared. The compressive strength and Young's modulus of elasticity of cylindrical specimens were 4.94% and 1.23% higher, respectively, in GPC compared to OPC concrete. Afterwards, the wall panels were tested incorporating each of the materials. The seismic characteristics of conventional concrete bare frame and geopolymer concrete bare frame showed good concordance with each other. The GPC frame exhibited better lateral properties than the traditional concrete frame. This initial stiffness calculated in the case of the GPC frame was 8.77 kN/mm which was 3.5% higher than the corresponding value of the OPC frame, 8.47 kN/mm. The maximum lateral load borne by both types was very similar, i.e., 25.51 kN by GPC-BF and 25.39 kN by OPC-BF. Similarly, the GPC confined masonry wall showed improved seismic properties compared to the cement concrete wall. The ultimate load capacity of the GPC-CM wall was 1.66 times the cracking load, whereas the OPC-CM wall was 1.52 times the cracking load, indicating that the GPC-CM wall bears more percentage load from the initiation of cracks until failure. The GPC wall resisted up to 119.1 kN load while the OPC wall resisted up to 114.3 kN of lateral load. Although the difference of 4.2% is small, it might be considered enough to offer GPC confinement as an environmentally-friendly alternative to conventional concrete. The failure mode was

identified as shear failure in both walls with no separation at the toothed interface between the tie-column and the masonry panel, demonstrating the superiority of the confined masonry compared to the infill masonry structures. The numerical models of the two confined masonry walls were well-validated by the experimental results.

The research suggests that alkali-activated fly-ash-based geopolymer concrete is a good substitute for OPC concrete and should be preferred in various applications to reduce the global usage of OPC and mitigate its detrimental environmental effects. The structural response of geopolymer concrete confined masonry made from fly ash is comparable to that of OPC concrete, indicating that the current engineered masonry design can be comfortably adopted, especially in highly seismic-prone areas, to produce a green environment. However, additional research is necessary to develop well-grounded seismic design criteria to predict the lateral in-plane load strength for GPC confined masonry structures with multiple stories.

**Author Contributions:** Conceptualization, M.M.A. and A.U.Q.; Methodology, M.M.A., A.U.Q., A.A. and S.A.; Software, M.M.A.; Validation, M.M.A., A.U.Q. and M.J.M.; Formal analysis, M.M.A., S.M.S.K. and A.A.; Investigation, A.U.Q. and A.A.; Data curation, A.A.; Writing—review and editing, M.M.A., U.A.M. and S.A.; Supervision, A.U.Q. and A.A. All authors have read and agreed to the published version of the manuscript.

**Funding:** This research received no external funding.

**Data Availability Statement:** Complete data has not been shared due to on-going PhD research work.

**Acknowledgments:** The authors would like to thank Asif Hameed, Test Floor Laboratory and Burhan Shareef, Concrete Laboratory at UET Lahore for the successful completion of experimental work from casting to testing. The authors also wish to express their gratitude to Rashid Hameed for his cooperation regarding equipment. Special thanks to the laboratory staff including Afzaal, Umer, Hamza, Touseef, Shahid, Faisal, Nadeem, Zahoor, Mahmood, who have helped in undertaking the necessary arrangements for the test setups.

**Conflicts of Interest:** The authors declare no conflict of interest.

## References

1. Almssad, A.; Almusaed, A.; Homod, R.Z. Masonry in the Context of Sustainable Buildings: A Review of the Brick Role in Architecture. *Sustainability* **2022**, *14*, 14734. [[CrossRef](#)]
2. Borah, B.; Kaushik, H.B.; Singhal, V. Lateral load-deformation models for seismic analysis and performance-based design of confined masonry walls. *J. Build. Eng.* **2022**, *48*, 103978. [[CrossRef](#)]
3. Macabuag, J.; Guragain, R.; Bhattacharya, S. Seismic retrofitting of non-engineered masonry in rural Nepal. *Proc. Inst. Civ. Eng. Build.* **2012**, *165*, 273–286. [[CrossRef](#)]
4. Bhattacharya, S.; Nayak, S.; Dutta, S.C. A critical review of retrofitting methods for unreinforced masonry structures. *Int. J. Disaster Risk Reduct.* **2014**, *7*, 51–67. [[CrossRef](#)]
5. Varela-Rivera, J.; Fernandez-Baqueiro, L.; Gamboa-Villegas, J.; Prieto-Coyoc, A.; Moreno-Herrera, J. Flexural behavior of confined masonry walls subjected to in-plane lateral loads. *Earthq. Spectra* **2019**, *35*, 405–422. [[CrossRef](#)]
6. Bruneau, M. State-of-the-art report on seismic performance of unreinforced masonry buildings. *J. Struct. Eng.* **1994**, *120*, 230–251. [[CrossRef](#)]
7. So, E.K.M.; Pomonis, A. Derivation of globally applicable casualty rates for use in earthquake loss estimation models. In Proceedings of the 15th World Conference on Earthquake Engineering, USB, Lisbon, Portugal, 24–28 September 2012.
8. Asian Development Bank and World Bank (ADB-WB). *Preliminary Damage and Needs Assessment-Pakistan 2005 Earthquake*; Asian Development Bank and World Bank: Islamabad, Pakistan, 2005.
9. Naseer, A.; Khan, A.N.; Hussain, Z.; Ali, Q. Observed seismic behavior of buildings in northern Pakistan during the 2005 Kashmir earthquake. *Earthq. Spectra* **2010**, *26*, 425–449. [[CrossRef](#)]
10. Marques, R.; Lourenço, P.B. A model for pushover analysis of confined masonry structures: Implementation and validation. *Bull. Earthq. Eng.* **2013**, *11*, 2133–2150. [[CrossRef](#)]
11. Meli, R. Structural design of masonry buildings: The Mexican practice. *Spec. Publ.* **1994**, *147*, 239–262.
12. Gallegos, H. Masonry in Peru. *Spec. Publ.* **1994**, *147*, 307–332.
13. Alcocer, S.M.; Klingner, R.E. Masonry research in the Americas. *Spec. Publ.* **1994**, *147*, 127–170.
14. Hidalgo, P.A. Seismic behavior and earthquake-resistant design of masonry buildings in Chile. *Spec. Publ.* **1994**, *147*, 333–356.
15. Garcia, L.E.; Yamin, L.E. Review of Masonry Construction in Columbia. *Spec. Publ.* **1994**, *147*, 283–306.

16. ElGawady, M.; Lestuzzi, P.; Badoux, M. A review of conventional seismic retrofitting techniques for URM. In Proceedings of the 13th International Brick and Block Masonry Conference, Amsterdam, The Netherlands, 4–7 July 2004; pp. 1–10.
17. Tomazevic, M. *Earthquake-Resistant Design of Masonry Buildings*; World Scientific: Singapore, 1999; Volume 1.
18. Brzev, S.; Meli, R. International guideline for seismic design of low-rise confined masonry buildings in regions of high seismic risk. In Proceedings of the 15th World Conference Earthquake Engineering, Lisbon, Portugal, 24–28 September 2012.
19. Yekrangnia, M.; Bakhshi, A.; Ghannad, M.A. Force-displacement model for solid confined masonry walls with shear-dominated failure mode. *Earthq. Eng. Struct. Dyn.* **2017**, *46*, 2209–2234. [[CrossRef](#)]
20. Najafgholipour, M.A.; Maheri, M.R.; Khajepour, M. Performance of confined masonry buildings in November 2017, Sarpole Zahab earthquake (Mw = 7.3), Iran. *Bull. Earthq. Eng.* **2022**, *20*, 4065–4095. [[CrossRef](#)]
21. Boen, T.; Pribadi, K.S. Engineering the non-engineered houses for better earthquake resistance in Indonesia. In Proceedings of the DRH Contents Meeting-EDMNIED 2007, Kobe, Japan, 12–13 March 2007; Volume 7.
22. Qazi, A.U.; Rasool, A.M.; Ibrahim, Y.E.; Hameed, A.; Ali, M.F. Behavior of Scaled Infilled Masonry, Confined Masonry & Reinforced Concrete Structures under Dynamic Excitations. *Buildings* **2022**, *12*, 774.
23. Hori, N.; Inoue, N.; Purushotam, D.; Nishida, T.; Kobayashi, J. Experimental and analytical studies on earthquake resisting behaviour of confined concrete block masonry structures. *Earthq. Eng. Struct. Dyn.* **2006**, *35*, 1699–1719. [[CrossRef](#)]
24. Marques, R.; Lourenço, P.B. Structural behaviour and design rules of confined masonry walls: Review and proposals. *Constr. Build. Mater.* **2019**, *217*, 137–155. [[CrossRef](#)]
25. Huang, L.; Lu, Y.; Yan, L.; Kasal, B.; Wang, L.; Zhang, T. Seismic performance of mortarless reinforced masonry walls. *J. Build. Eng.* **2020**, *31*, 101368. [[CrossRef](#)]
26. Jain, S.K.; Basu, D.; Ghosh, I.; Rai, D.C.; Brzev, S.; Bhargava, L.K. Application of confined masonry in a major project in India. In Proceedings of the NCEE 2014–10th U.S. National Conference on Earthquake Engineering Frontiers of Earthquake Engineering, Anchorage, AK, USA, 21–25 July 2014. [[CrossRef](#)]
27. Zhou, Y.; Zheng, S.; Chen, L.; Long, L.; Dong, L. Mechanical properties and seismic behavior of confined masonry walls in freeze-thaw environment. *Structures* **2021**, *31*, 647–659. [[CrossRef](#)]
28. Yoshimura, K.; Kikuchi, K.; Kuroki, M.; Nonaka, H.; Kim, K.T.; Wangdi, R.; Oshikata, A. Experimental study for developing higher seismic performance of brick masonry walls. In Proceedings of the 13th World Conference on Earthquake Engineering, Vancouver, BC, Canada, 1–6 August 2004. Paper, 1597.
29. Tomaževič, M.; Klemenc, I. Seismic behaviour of confined masonry walls. *Earthq. Eng. Struct. Dyn.* **1997**, *26*, 1059–1071. [[CrossRef](#)]
30. Borah, B.; Singhal, V.; Kaushik, H.B. Sustainable housing using confined masonry buildings. *SN Appl. Sci.* **2019**, *1*, 983. [[CrossRef](#)]
31. Erberik, M.A.; Citiloglu, C.; Erkoseoglu, G. Seismic performance assessment of confined masonry construction at component and structure levels. *Bull. Earthq. Eng.* **2019**, *17*, 867–889. [[CrossRef](#)]
32. Gouveia, J.P.; Lourenço, P.B. Masonry shear walls subjected to cyclic loading: Influence of confinement and horizontal reinforcement. In Proceedings of the North American Masonry Conference, St. Luis, MI, USA, 3–5 June 2007.
33. Brzev, S. *Earthquake-Resistant Confined Masonry Construction*; NICEE, National Information Center of Earthquake Engineering, IIT Kanpur: Kanpur, India, 2007.
34. Sharma, P.; Verma, M.; Sharma, N. Examine the mechanical properties of recycled coarse aggregate with MK GGBS. In Proceedings of the IOP Conference Series: Materials Science and Engineering, Sanya, China, 2–14 November 2021; Volume 1116, p. 12152.
35. Verma, M.; Sharma, N.; Sharma, P.; Singh, P. Evaluate the Effect in Terms of Setting Time and Compressive Strength of Oleic Acid as an Admixture in Cement. *Test Eng. Manag.* **2020**, *12422*, 12422–12427.
36. Nagar, P.A.; Gupta, N.; Kishore, K.; Parashar, A.K. Coupled effect of B. Sphaericus bacteria and calcined clay mineral on OPC concrete. *Mater. Today Proc.* **2021**, *44*, 113–117. [[CrossRef](#)]
37. Kishore, K.; Gupta, N. Application of domestic & industrial waste materials in concrete: A review. *Mater. Today Proc.* **2020**, *26*, 2926–2931.
38. Sharma, P.; Sharma, N.; Singh, P.; Verma, M.; Parihar, H.S. Examine the effect of setting time and compressive strength of cement mortar paste using iminodiacetic acid. *Mater. Today Proc.* **2020**, *32*, 878–881. [[CrossRef](#)]
39. Gupta, N.; Gupta, A.; Saxena, K.K.; Shukla, A.; Goyal, S.K. Mechanical and durability properties of geopolymer concrete composite at varying superplasticizer dosage. *Mater. Today Proc.* **2021**, *44*, 12–16. [[CrossRef](#)]
40. Barcelo, L.; Kline, J.; Walenta, G.; Gartner, E. Cement and carbon emissions. *Mater. Struct.* **2014**, *47*, 1055–1065. [[CrossRef](#)]
41. Bosoaga, A.; Masek, O.; Oakey, J.E. CO<sub>2</sub> capture technologies for cement industry. *Energy Procedia* **2009**, *1*, 133–140. [[CrossRef](#)]
42. Malhotra, V.M. Introduction: Sustainable development and concrete technology. *Concr. Int.* **2002**, *24*, 7.
43. Yıldırım, G.; Kul, A.; Özçelicki, E.; Şahmaran, M.; Aldemir, A.; Figueira, D.; Ashour, A. Development of alkali-activated binders from recycled mixed masonry-originated waste. *J. Build. Eng.* **2021**, *33*, 101690. [[CrossRef](#)]
44. Aprianti, E.; Shafigh, P.; Bahri, S.; Farahani, J.N. Supplementary cementitious materials origin from agricultural wastes—A review. *Constr. Build. Mater.* **2015**, *74*, 176–187. [[CrossRef](#)]
45. Kishore, K.; Gupta, N. Mechanical characterization and assessment of composite geopolymer concrete. *Mater. Today Proc.* **2021**, *44*, 58–62. [[CrossRef](#)]
46. Parashar, A.K.; Gupta, A. Investigation of the effect of bagasse ash, hooked steel fibers and glass fibers on the mechanical properties of concrete. *Mater. Today Proc.* **2021**, *44*, 801–807. [[CrossRef](#)]

47. Parashar, A.K.; Gupta, A. Experimental study of the effect of bacillus megaterium bacteria on cement concrete. *IOP Conf. Ser. Mater. Sci. Eng.* **2021**, *1116*, 12168. [[CrossRef](#)]
48. Mehta, P.K. *Concrete Technology for a Sustainable Development in the 21st Century*; CRC Press: Boca Raton, FL, USA, 1999; Volume 83.
49. Van Oss, H.G.; Padovani, A.C. Cement manufacture and the environment part II: Environmental challenges and opportunities. *J. Ind. Ecol.* **2003**, *7*, 93–126.
50. Li, C.; Gong, X.Z.; Cui, S.P.; Wang, Z.H.; Zheng, Y.; Chi, B.C. CO<sub>2</sub> emissions due to cement manufacture. *Mater. Sci. Forum* **2011**, *685*, 181–187. [[CrossRef](#)]
51. De Brito, J.; Saikia, N. *Recycled Aggregate in Concrete: Use of Industrial, Construction and Demolition Waste*; Springer Science & Business Media: Berlin/Heidelberg, Germany, 2012.
52. Diaz-Loya, E.I.; Allouche, E.N.; Vaidya, S. Mechanical properties of fly-ash-based geopolymer concrete. *ACI Mater. J.* **2011**, *108*, 300.
53. Yildirim, H.; Sümer, M.; Akyüncü, V.; Gürbüz, E. Comparison on efficiency factors of F and C types of fly ashes. *Constr. Build. Mater.* **2011**, *25*, 2939–2947. [[CrossRef](#)]
54. Duxson, P.; Provis, J.L.; Lukey, G.C.; Van Deventer, J.S.J. The role of inorganic polymer technology in the development of 'green concrete'. *Cem. Concr. Res.* **2007**, *37*, 1590–1597. [[CrossRef](#)]
55. Albitar, M.; Ali, M.S.M.; Visintin, P. Experimental study on fly ash and lead smelter slag-based geopolymer concrete columns. *Constr. Build. Mater.* **2017**, *141*, 104–112. [[CrossRef](#)]
56. Kaya, M.; Koksall, F.; Gencil, O.; Munir, M.J.; Kazmi, S.M.S. Influence of micro Fe<sub>2</sub>O<sub>3</sub> and MgO on the physical and mechanical properties of the zeolite and kaolin based geopolymer mortar. *J. Build. Eng.* **2022**, *52*, 104443. [[CrossRef](#)]
57. Panagiotopoulou, C.; Kontori, E.; Perraki, T.; Kakali, G. Dissolution of aluminosilicate minerals and by-products in alkaline media. *J. Mater. Sci.* **2007**, *42*, 2967–2973. [[CrossRef](#)]
58. Rangan, B.V. *Fly Ash-Based Geopolymer Concrete*; Curtin University of Technology: Perth, WA, Australia, 2008.
59. Marín-López, C.; Araiza, J.L.R.; Manzano-Ramírez, A.; Avalos, J.C.R.; Perez-Bueno, J.J.; Muñoz-Villareal, M.S.; Ventura-Ramos, E.; Vorobiev, Y. Synthesis and characterization of a concrete based on metakaolin geopolymer. *Inorg. Mater.* **2009**, *45*, 1429–1432. [[CrossRef](#)]
60. Okoye, F.N.; Durgaprasad, J.; Singh, N.B. Effect of silica fume on the mechanical properties of fly ash based-geopolymer concrete. *Ceram. Int.* **2016**, *42*, 3000–3006. [[CrossRef](#)]
61. Mathew, B.J.; Sudhakar, M.; Natarajan, C. Strength, economic and sustainability characteristics of coal ash-GGBS based geopolymer concrete. *Int. J. Comput. Eng. Res.* **2013**, *3*, 207–212.
62. Detphan, S.; Chindaprasirt, P. Preparation of fly ash and rice husk ash geopolymer. *Int. J. Miner. Metall. Mater.* **2009**, *16*, 720–726.
63. Ojha, A.; Aggarwal, P. Fly ash based geopolymer concrete: A comprehensive review. *Silicon* **2022**, *14*, 2453–2472. [[CrossRef](#)]
64. Huang, Y.-J.; Guo, F.; Zhang, H.; Yang, Z. An Efficient Computational Framework for Generating Realistic 3D Mesoscale Concrete Models Using Micro X-Ray Computed Tomography Images and Dynamic Physics Engine. *Cem. Concr. Compos.* **2022**, *126*, 104347. [[CrossRef](#)]
65. Albitar, M.; Visintin, P.; Ali, M.S.M.; Lavigne, O.; Gamboa, E. Bond slip models for uncorroded and corroded steel reinforcement in class-F fly ash geopolymer concrete. *J. Mater. Civ. Eng.* **2017**, *29*, 4016186. [[CrossRef](#)]
66. Yu, R.; Spiesz, P.; Brouwers, H.J.H. Development of an eco-friendly Ultra-High Performance Concrete (UHPC) with efficient cement and mineral admixtures uses. *Cem. Concr. Compos.* **2015**, *55*, 383–394. [[CrossRef](#)]
67. Sugama, T.; Pyatina, T. Effect of sodium carboxymethyl celluloses on water-catalyzed self-degradation of 200 °C-heated alkali-activated cement. *Cem. Concr. Compos.* **2015**, *55*, 281–289. [[CrossRef](#)]
68. Ioannou, S.; Paine, K.; Reig, L.; Quillin, K. Performance characteristics of concrete based on a ternary calcium sulfoaluminate-anhydrite-fly ash cement. *Cem. Concr. Compos.* **2015**, *55*, 196–204. [[CrossRef](#)]
69. Albitar, M.; Visintin, P.; Ali, M.S.M.; Drechsler, M. Assessing behaviour of fresh and hardened geopolymer concrete mixed with class-F fly ash. *KSCE J. Civ. Eng.* **2015**, *19*, 1445–1455. [[CrossRef](#)]
70. Laskar, A.I.; Bhattacharjee, R. Effect of Plasticizer and Superplasticizer on Rheology of Fly-Ash-Based Geopolymer Concrete. *ACI Mater. J.* **2013**, *110*, 5.
71. Albitar, M.; Ali, M.S.M.; Visintin, P.; Drechsler, M. Effect of granulated lead smelter slag on strength of fly ash-based geopolymer concrete. *Constr. Build. Mater.* **2015**, *83*, 128–135. [[CrossRef](#)]
72. Fan, X.; Zhang, M. Experimental study on flexural behaviour of inorganic polymer concrete beams reinforced with basalt rebar. *Compos. Part B Eng.* **2016**, *93*, 174–183. [[CrossRef](#)]
73. Kathirvel, P.; Kaliyaperumal, S.R.M. Influence of recycled concrete aggregates on the flexural properties of reinforced alkali activated slag concrete. *Constr. Build. Mater.* **2016**, *102*, 51–58. [[CrossRef](#)]
74. Maranan, G.B.; Manalo, A.C.; Benmokrane, B.; Karunasena, W.; Mendis, P. Behavior of concentrically loaded geopolymer-concrete circular columns reinforced longitudinally and transversely with GFRP bars. *Eng. Struct.* **2016**, *117*, 422–436. [[CrossRef](#)]
75. Yost, J.R.; Radlińska, A.; Ernst, S.; Salera, M. Structural behavior of alkali activated fly ash concrete. Part 1: Mixture design, material properties and sample fabrication. *Mater. Struct.* **2013**, *46*, 435–447. [[CrossRef](#)]
76. ASTM C127-88(2001); Standard Test Method for Specific Gravity and Absorption of Coarse Aggregate 1; no. Reapproved. ASTM: West Conshohocken: PA, USA, 2001; Volume 4, pp. 1–5.

77. Ghafoor, M.T.; Khan, Q.S.; Qazi, A.U.; Sheikh, M.N.; Hadi, M.N.S. Influence of alkaline activators on the mechanical properties of fly ash based geopolymer concrete cured at ambient temperature. *Constr. Build. Mater.* **2021**, *273*, 121752. [CrossRef]
78. ASTM C 136-06; Standard Test Method for Sieve Analysis of Fine and Coarse Aggregates. ASTM: West Conshohocken, PA, USA, 2006; pp. 1–5. [CrossRef]
79. ASTM C67-07; Standard Test Methods for Sampling and Testing Brick and Structural Clay Tile. ASTM International: West Conshohocken, PA, USA, 2007; Volume i, pp. 1–12. Available online: [www.astm.org](http://www.astm.org) (accessed on 15 September 2022).
80. ASTM C109; ASTM C109/C109M-20b: Standard Test Method for Compressive Strength of Hydraulic Cement Mortars (Using 2-inor [50 mm] Cube Specimens). Annual Book of ASTM Standards; ASTM: West Conshohocken, PA, USA, 2020; Volume 4, p. 9.
81. Masonry Standards Joint Committee (MSJC) of the Masonry Society. *Building Code Requirements for Masonry Structures (TMS 402-11/ACI 530-11/ASCE 6-11) and Specification for Masonry Structures (TMS 602-11/ACI 530.1-11/ASCE 5-11) and Companion Commentaries*; American Concrete Institute: Farmington Hills, MI, USA, 2011.
82. ASTM C39/C39M; Standard Test Method for Compressive Strength of Cylindrical Concrete Specimens 1. ASTM Stand. B; ASTM: West Conshohocken: PA, USA, 2003; Volume i, no. March. pp. 1–5.
83. ASTM C469/C469M-10; Standard Test Method for Static Modulus of Elasticity and Poisson's Ratio of Concrete in Compression. ASTM Stand. C; ASTM: West Conshohocken, PA, USA, 2010; Volume 469.
84. IS 1608-2005; Metallic Materials-Tensile Testing at Ambient Temperature. Bur. Indian Stand.; Instron: Norwood, MA, USA, 2005.
85. Lourenço, P.B. Computational Strategies for Masonry Structures. Doctoral Thesis, Delft University of Technology, Delft, The Netherlands, 1996.
86. Kömürçü, S.; Gedikli, A. Macro and Micro Modelling of the Unreinforced Masonry Shear Walls. *Eur. J. Eng. Nat. Sci.* **2019**, *3*, 116–123. Available online: <https://dergipark.org.tr/en/pub/ejens/issue/49410/369461> (accessed on 15 September 2022).
87. Mynarz, M.; Mynarzova, L. Non-linear approaches to the response of brick masonry wall to lateral loading. *Int. J. GEOMATE* **2018**, *14*, 76–82. [CrossRef]
88. Dhanasekar, M.; Elsalakawy, T. IJERT-Numerical Simulation of Masonry Prism Test Using ANSYS and ABAQUS Related Papers Review of Modelling of Masonry Shear Numerical Simulation of Masonry Prism Test Using ANSYS and ABAQUS. *IJERT J. Int. J. Eng. Res. Technol.* **2015**, *4*. Available online: [www.ijert.org](http://www.ijert.org) (accessed on 15 September 2022).
89. Kanit, R.; Döndüren, M.S. Investigation of Using Ansys Software in the Determination of Stress Behaviours of Masonry Walls under out of Plane Cycling Load. *Int. J. Phys. Sci.* **2010**, *5*, 97–108. Available online: <http://www.academicjournals.org/IJPS> (accessed on 15 September 2022).
90. Magenes, G.; Della Fontana, A. Simplified non-linear seismic analysis of masonry buildings. *Proc. Br. Masonry Soc.* **1998**, *8*, 190–195.
91. Vanin, A.; Foraboschi, P. Journal-Modelling of Masonry Panels by Truss Analogy–Part 1. *Mason. Int.* **2009**, *22*, 1.
92. Tomažević, M.; Gams, M. Shaking table study and modelling of seismic behaviour of confined AAC masonry buildings. *Bull. Earthq. Eng.* **2012**, *10*, 863–893. [CrossRef]
93. Lagomarsino, S.; Penna, A.; Galasco, A.; Cattari, S. TREMURI program: An equivalent frame model for the nonlinear seismic analysis of masonry buildings. *Eng. Struct.* **2013**, *56*, 1787–1799. [CrossRef]
94. Caliò, I.; Marletta, M.; Pantò, B. A new discrete element model for the evaluation of the seismic behaviour of unreinforced masonry buildings. *Eng. Struct.* **2012**, *40*, 327–338. [CrossRef]
95. Ansys Inc. "Element Reference," Volume 15317, No. November, p. 9, 2010. Available online: [https://www.mm.bme.hu/~gyebro/files/fea/ansys/ansys\\_13\\_element\\_reference.pdf](https://www.mm.bme.hu/~gyebro/files/fea/ansys/ansys_13_element_reference.pdf) (accessed on 25 September 2022).
96. Neupane, K.; Kidd, P.; Chalmers, D.; Baweja, D.; Shrestha, R. Investigation on compressive strength development and drying shrinkage of ambient cured powder-activated geopolymer concretes. *Aust. J. Civ. Eng.* **2016**, *14*, 72–83. [CrossRef]
97. Reddy, P.C.; Ganesan, R. Comparative study of compressive strength of novel steel fiber reinforced geopolymer concrete and conventional concrete. *Mater. Today Proc.* **2023**, *77*, 504–508. [CrossRef]
98. Razak, S.; Zainal, F.F.; Shamsudin, S.R. Effect of porosity and water absorption on compressive strength of fly ash based geopolymer and OPC Paste. *IOP Conf. Ser. Mater. Sci. Eng.* **2020**, *957*, 12035. [CrossRef]
99. Bondar, D.; Lynsdale, C.J.; Milestone, N.B.; Hassani, N.; Ramezani-pour, A.A. Engineering properties of alkali-activated natural pozzolan concrete. *ACI Mater. J.* **2011**, *108*, 64–72.
100. Olivia, M.; Nikraz, H. Properties of fly ash geopolymer concrete designed by Taguchi method. *Mater. Des.* **2012**, *36*, 191–198. [CrossRef]
101. Nath, P.; Sarker, P.K. Flexural strength and elastic modulus of ambient-cured blended low-calcium fly ash geopolymer concrete. *Constr. Build. Mater.* **2017**, *130*, 22–31. [CrossRef]
102. Ganesan, N.; Indira, P.V.; Irshad, P. Effect of ferrocement infill on the strength and behavior of RCC frames under reverse cyclic loading. *Eng. Struct.* **2017**, *151*, 273–281. [CrossRef]
103. Li, B.; Wang, J.; Duan, M.; Guo, L.; Wang, B. Cyclic experimental and numerical analytical investigation of precast concrete frames with buckling-restrained braces considering various assembling connections. *Structures* **2021**, *34*, 1135–1153. [CrossRef]
104. Lyu, H.; Deng, M.; Ma, Y.; Yang, S.; Cheng, Y. In-plane cyclic tests on strengthening of full-scale autoclaved aerated concrete blocks infilled RC frames using highly ductile concrete (HDC). *J. Build. Eng.* **2022**, *49*, 104083. [CrossRef]
105. Sumajouw, D.M.J.; Hardjito, D.; Wallah, S.E.; Rangan, B.V. Fly ash-based geopolymer concrete: Study of slender reinforced columns. *J. Mater. Sci.* **2007**, *42*, 3124–3130. [CrossRef]

106. Rahman, M.; Sarker, P. Geopolymer concrete columns under combined axial load and biaxial bending. In Proceedings of the Concrete 2011 Conference, Perth, WA, Australia, 12 October 2011.
107. Borah, B.; Singhal, V.; Kaushik, H.B. Assessment of seismic design provisions for confined masonry using experimental and numerical approaches. *Eng. Struct.* **2021**, *245*, 112864. [[CrossRef](#)]
108. El-Diasity, M.; Okail, H.; Kamal, O.; Said, M. Structural performance of confined masonry walls retrofitted using ferrocement and GFRP under in-plane cyclic loading. *Eng. Struct.* **2015**, *94*, 54–69. [[CrossRef](#)]
109. Ahmed, A.; Ahmad, I.; Shahzada, K.; Naqash, M.T.; Alam, B.; Fahad, M.; Khan, S.W. Seismic Capacity Assessment of Confined Brick Masonry Building: An Experimental Approach. *Shock. Vib.* **2018**, *2018*, 4756352. [[CrossRef](#)]
110. Giofrè, M.; Cavalagli, N.; Gusella, V.; Pepi, C. Confined vs. unreinforced masonry: Construction and shaking table tests of two-storey buildings. *Constr. Build. Mater.* **2022**, *333*, 126961. [[CrossRef](#)]
111. *ASCE/SEI 41-06; Supplement to Seismic Rehabilitation of Existing Buildings*. ASCE: Reston, VA, USA, 2007.
112. Ashraf, M. Development of Low-Cost and Efficient Retrofitting Technique for Unreinforced Masonry Buildings. Ph.D. Dissertation, University of Engineering and Technology, Peshawar, Pakistan, 2010.
113. Reboul, N.; Mesticou, Z.; Larbi, A.S.; Ferrier, E. Experimental study of the in-plane cyclic behaviour of masonry walls strengthened by composite materials. *Constr. Build. Mater.* **2018**, *164*, 70–83. [[CrossRef](#)]
114. Hasnat, A.; Ahsan, R.; Yashin, S.M. Quasi-static in-plane behavior of full-scale unreinforced masonry walls retrofitted using ferro-cement overlay. *Asian J. Civ. Eng.* **2022**, *23*, 649–664. [[CrossRef](#)]
115. Konthesingha, K.M.C.; Masia, M.J.; Petersen, R.B.; Page, A.W. Experimental evaluation of static cyclic in-plane shear behavior of unreinforced masonry walls strengthened with NSM FRP strips. *J. Compos. Constr.* **2015**, *19*, 4014055. [[CrossRef](#)]
116. Mojsilović, N.; Simundic, G.; Page, A. Masonry wallettes with damp-proof course membrane subjected to cyclic shear: An experimental study. *Constr. Build. Mater.* **2010**, *24*, 2135–2144. [[CrossRef](#)]
117. Aguilar, G.; Meli, R.; Diaz, R.; Vázquez-del-Mercado, R. Influence of horizontal reinforcement on the behavior of confined masonry walls. In Proceedings of the Eleventh World Conference on Earthquake Engineering, Acapulco, Mexico, 23–28 June 1996.
118. Yáñez, F.; Astroza, M.; Holmberg, A.; Ogaz, O. Behavior of confined masonry shear walls with large openings. In Proceedings of the 13th World Conference on Earthquake Engineering, Vancouver, BC, Canada, 1–6 August 2004; Volume 3438.
119. Marinilli, A.; Castilla, E. Experimental evaluation of confined masonry walls with several confining-columns. In Proceedings of the 13th World Conference on Earthquake Engineering, Vancouver, BC, Canada, 1–6 August 2004.
120. Zabala, F.; Bustos, J.L.; Masanet, A.; Santalucia, J. Experimental behaviour of masonry structural walls used in Argentina. In Proceedings of the 13th World Conference on Earthquake Engineering, Vancouver, BC, Canada, 1–6 August 2004.
121. Bourzam, A.; Goto, T.; Miyajima, M. Shear capacity prediction of confined masonry walls subjected to cyclic lateral loading. *Doboku Gakkai Ronbunshuu A* **2008**, *64*, 692–704. [[CrossRef](#)]
122. Gavilan, J.J.P.; Flores, L.E.; Alcocer, S.M. An experimental study of confined masonry walls with varying aspect ratios. *Earthq. Spectra* **2015**, *31*, 945–968. [[CrossRef](#)]
123. Tena-Colunga, A.; Juárez-Ángeles, A.; Salinas-Vallejo, V.H. Cyclic behavior of combined and confined masonry walls. *Eng. Struct.* **2009**, *31*, 240–259. [[CrossRef](#)]
124. Kuang, J.S.; Wang, Z. Cyclic load tests of rc frame with column-isolated masonry infills. In Proceedings of the Second European Conference on Earthquake Engineering and Seismology, Istanbul, Turkey, 25–29 August 2014; pp. 25–29.
125. Ozkaynak, H.; Yuksel, E.; Buyukozturk, O.; Yalcin, C.; Dindar, A.A. Quasi-static and pseudo-dynamic testing of infilled RC frames retrofitted with CFRP material. *Compos. Part B Eng.* **2011**, *42*, 238–263. [[CrossRef](#)]
126. Van, T.C.; Lau, T.L. Experimental evaluation of reinforced concrete frames with unreinforced masonry infills under monotonic and cyclic loadings. *Int. J. Civ. Eng.* **2021**, *19*, 401–419. [[CrossRef](#)]
127. Li, Y.; Zhu, J.; Wang, Z. Investigation on mechanical properties of masonry infill wall strengthened with ECC. *KSCE J. Civ. Eng.* **2019**, *23*, 295–306. [[CrossRef](#)]
128. Durrani, A.J.; Haider, S. Seismic response of R/C frames with unreinforced masonry infills. In Proceedings of the 11th World Conference on Earthquake Engineering, Acapulco, Mexico, 23–28 June 1996.
129. Jiang, H.; Liu, X.; Mao, J. Full-scale experimental study on masonry infilled RC moment-resisting frames under cyclic loads. *Eng. Struct.* **2015**, *91*, 70–84. [[CrossRef](#)]
130. Peng, Q.; Zhou, X.; Yang, C. Influence of connection and constructional details on masonry-infilled RC frames under cyclic loading. *Soil Dyn. Earthq. Eng.* **2018**, *108*, 96–110. [[CrossRef](#)]
131. Penava, D.; Sarhosis, V.; Kožar, I.; Guljaš, I. Contribution of RC columns and masonry wall to the shear resistance of masonry infilled RC frames containing different in size window and door openings. *Eng. Struct.* **2018**, *172*, 105–130. [[CrossRef](#)]
132. Aldred, J.; Day, J. Is geopolymer concrete a suitable alternative to traditional concrete. In Proceedings of the 37th Conference on Our World in Concrete & Structures, Singapore, 29–31 August 2012; pp. 29–31.
133. Munir, M.J.; Kazmi, S.M.S.; Khitab, A.; Hassan, M. Utilization of rice husk ash to mitigate alkali silica reaction in concrete. In Proceedings of the 2nd International Multi-Disciplinary Conference (IMDC 2016), University of Lahore (Gujrat Campus), Gujrat, Pakistan, 19–20 December 2016; pp. 1–3.

134. Munir, M.J.; Abbas, S.; Qazi, A.U.; Nehdi, M.L.; Kazmi, S.M.S. Role of test method in detection of alkali–silica reactivity of concrete aggregates. *Proc. Inst. Civ. Eng.–Constr. Mater.* **2018**, *171*, 203–221. [[CrossRef](#)]
135. Munir, M.J.; Kazmi, S.M.S.; Wu, Y.F.; Lin, X. Axial stress-strain performance of steel spiral confined acetic acid immersed and mechanically rubbed recycled aggregate concrete. *J. Build. Eng.* **2021**, *34*, 101891. [[CrossRef](#)]

**Disclaimer/Publisher’s Note:** The statements, opinions and data contained in all publications are solely those of the individual author(s) and contributor(s) and not of MDPI and/or the editor(s). MDPI and/or the editor(s) disclaim responsibility for any injury to people or property resulting from any ideas, methods, instructions or products referred to in the content.